Article

Three-dimensional flat bands in pyrochlore metal $CaNi_2$

https://doi.org/10.1038/s41586-023-06640-1

Received: 6 January 2023

Accepted: 13 September 2023

Published online: 8 November 2023

Check for updates

Joshua P. Wakefield[1,11], Mingu Kang[1,2,11], Paul M. Neves[1,11], Dongjin Oh[1,11], Shiang Fang[1], Ryan McTigue[1], S. Y. Frank Zhao[1], Tej N. Lamichhane[3], Alan Chen[1], Seongyong Lee[2,4], Sudong Park[2,4], Jae-Hoon Park[2,4], Chris Jozwiak[5], Aaron Bostwick[5], Eli Rotenberg[5], Anil Rajapitamahuni[6], Elio Vescovo[6], Jessica L. McChesney[7], David Graf[8], Johanna C. Palmstrom[9], Takehito Suzuki[10], Mingda Li[3], Riccardo Comin[1]✉ & Joseph G. Checkelsky[1]✉

Electronic flat-band materials host quantum states characterized by a quenched kinetic energy. These flat bands are often conducive to enhanced electron correlation effects and emergent quantum phases of matter[1]. Long studied in theoretical models[2–4], these systems have received renewed interest after their experimental realization in van der Waals heterostructures[5,6] and quasi-two-dimensional (2D) crystalline materials[7,8]. An outstanding experimental question is if such flat bands can be realized in three-dimensional (3D) networks, potentially enabling new materials platforms[9,10] and phenomena[11–13]. Here we investigate the C15 Laves phase metal $CaNi_2$, which contains a nickel pyrochlore lattice predicted at a model network level to host a doubly-degenerate, topological flat band arising from 3D destructive interference of electronic hopping[14,15]. Using angle-resolved photoemission spectroscopy, we observe a band with vanishing dispersion across the full 3D Brillouin zone that we identify with the pyrochlore flat band as well as two additional flat bands that we show arise from multi-orbital interference of Ni *d*-electrons. Furthermore, we demonstrate chemical tuning of the flat-band manifold to the Fermi level that coincides with enhanced electronic correlations and the appearance of superconductivity. Extending the notion of intrinsic band flatness from 2D to 3D, this provides a potential pathway to correlated behaviour predicted for higher-dimensional flat-band systems ranging from tunable topological[15] to fractionalized phases[16].

The notion of lattice geometry-enforced destructive quantum interference of electrons and the resulting suppression of electronic dispersion is essential for the development of flat-band materials[1,17,18]. This is exemplified in 2D by the kagome network (Fig. 1a). In this corner-sharing network of triangles, alternating-phase quasi-molecular orbitals on each hexagonal plaquette are trapped by the destructive interference of nearest-neighbour hopping pathways in the triangular plaquette. These are known as compact localized states (CLSs), and their degeneracy supports the emergence of a flat electronic band[17]. This mathematical concept has recently led to the experimental identification of topological flat bands in the *d*-electron kagome metals[8,19–21]. Being a natively 2D line graph model[22], however, the flatness of the kagome band once embedded in a 3D crystal structure is only maintained in the third dimension by a weakness of interlayer hopping t' because of, for example, a quasi-2D structure[23,24] (Fig. 1b). Furthermore, the topological states in such layered structures are inherently 2D in nature, presenting challenges for the realization of 3D topological flat-band models[25].

An intrinsically 3D flat-band lattice can be constructed by instead using a building block that extends the triangular plaquettes of the kagome lattice into the third dimension to form tetrahedra (Fig. 1c). Tiled alternatively within the building block, these tetrahedra enforce destructive interference in all three dimensions. Stacking this unit forms the pyrochlore lattice—a cubic network of corner-sharing tetrahedra that can be viewed as containing *ABC*-stacked kagome layers (Fig. 1d) as well as four (111) symmetry-equivalent dihedral kagome planes (Fig. 1e). This connectivity supports 3D CLSs (Fig. 1c) and flat bands that are dispersionless in all spatial directions (Fig. 1g) (mathematically, the pyrochlore is the 3D line graph of the diamond lattice[22]). The pyrochlore system has attracted attention as a host for various phenomena, including magnetism, superconductivity, topology and correlation physics[12,14,15,22,26–35]. Furthermore, within the framework of the single-orbital isotropic band model, this system has been predicted to support a doubly-degenerate flat band and Dirac nodal lines[15]. Despite these investigations, the applicability of the fundamental flat-band model has eluded concrete experimental confirmation.

[1]Department of Physics, Massachusetts Institute of Technology, Cambridge, MA, USA. [2]Center for Complex Phase Materials, Max Planck POSTECH/Korea Research Initiative, Pohang, Republic of Korea. [3]Department of Nuclear Science and Engineering, Massachusetts Institute of Technology, Cambridge, MA, USA. [4]Department of Physics, Pohang University of Science and Technology, Pohang, Republic of Korea. [5]Advanced Light Source, Lawrence Berkeley National Laboratory, Berkeley, CA, USA. [6]National Synchrotron Light Source II, Brookhaven National Laboratory, Upton, NY, USA. [7]X-ray Science Division, Advanced Photon Source, Argonne National Laboratory, Lemont, IL, USA. [8]National High Magnetic Field Laboratory, Tallahassee, FL, USA. [9]National High Magnetic Field Laboratory, LANL, Los Alamos, NM, USA. [10]Department of Physics, Toho University, Funabashi, Japan. [11]These authors contributed equally: Joshua P. Wakefield, Mingu Kang, Paul M. Neves, Dongjin Oh. ✉e-mail: rcomin@mit.edu; checkelsky@mit.edu

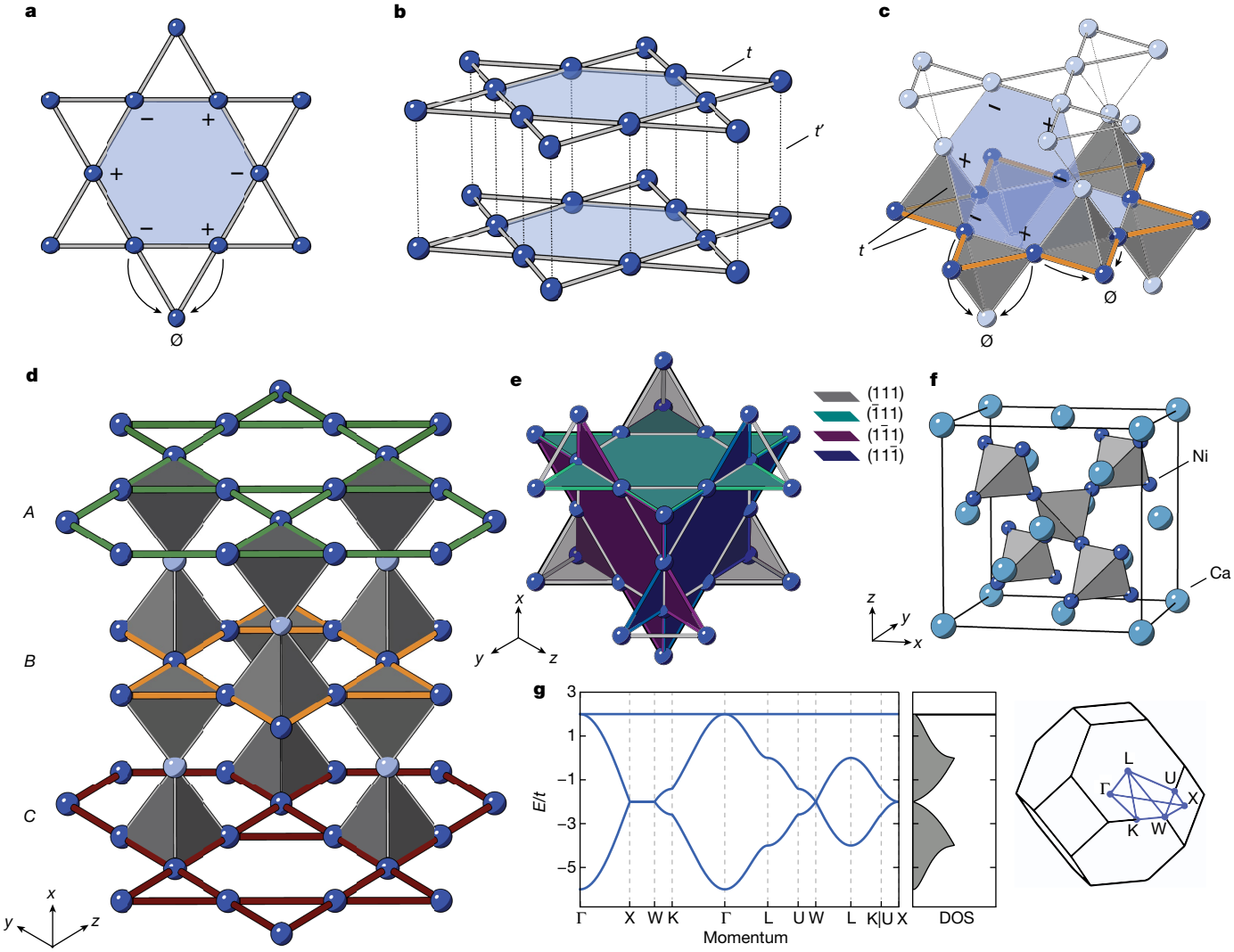

Fig. 1 | Kagome and pyrochlore flat-band states. a, Kagome lattice structure formed from corner-sharing triangles with compact localized state highlighted in blue. Destructive interference (Ø) arises from the cancellation between alternating quantum phases (+, −). **b**, Direct (*AA*) stacking of the kagome lattice into a 3D crystal with intralayer coupling labelled *t* and interlayer coupling labelled *t*′. **c**, 2D corner-sharing network of alternately directed tetrahedra forms a kagome lattice (orange) with the additional out-of-plane site creating a decorated kagome layer. Both in-plane hopping and out-of-plane hopping are destructively interfered. **d**, The resulting cubic pyrochlore lattice, composed of *ABC* stacking of kagome layers and interlayer triangular layers along the ⟨111⟩ direction. **e**, Alternative view of the pyrochlore lattice highlighting the four dihedral kagome planes. **f**, Crystal structure of $CaNi_2$ with Ni forming the pyrochlore sublattice. **g**, Tight-binding band structure of the pyrochlore lattice with the associated DOS and Brillouin zone.

Here we report a study of bulk single crystals of the C15 Laves phase $CaNi_2$ (space group $Fd\bar{3}m$), which hosts an Ni pyrochlore network[36] (Fig. 1f). Using angle-resolved photoemission spectroscopy (ARPES), quantum oscillations, density functional theory and tight-binding modelling, we comprehensively map the energy spectrum and Fermi surface and find a set of prominent flat electronic bands below the Fermi level (E_F). We show that the narrowest of these bands is related to the flat band intrinsic to the isotropic pyrochlore lattice realized in the Ni d_{z^2} orbital-hopping network. We show further that two additional flat bands appearing at higher and lower binding energies originate from the multiple destructive interference pathways among the Ni d_{xz}/d_{yz} and $d_{xy}/d_{x^2-y^2}$ orbitals, which, to our knowledge, has not previously been anticipated. This identifies $CaNi_2$ as a realization of the *d*-electron pyrochlore band structure and further suggests the C15 Laves phase intermetallics as a material family in which the confluence of flat bands, topology, magnetism and superconductivity on the pyrochlore lattice can be studied. Additionally, we show that in the isostructural system $Ca(Rh_{1-x}Ru_x)_2$, the higher-energy flat band is brought to E_F as observed by ARPES and thermodynamic measurements, concurrent with the appearance of superconductivity. These findings may both aid in understanding previously measured exotic states in pyrochlore materials[30] and suggest a route forward for band engineering superconducting and fractional quantum phases[28].

Pyrochlore flat bands in $CaNi_2$

Figure 2 summarizes our main vacuum ultraviolet (VUV) ARPES results on $CaNi_2$. Considering the 3D nature of the underlying pyrochlore lattice, we explored the electronic structure while continuously tuning the photon energy from 80 eV to 370 eV to vary the out-of-plane momentum k_z and map the full 3D Brillouin zone. The schematic in Fig. 2a shows the multiple 3D Brillouin zone configurations of $CaNi_2$ and how different momentum–space directions (colour-coded dashed lines) intersect the high-symmetry points. The energy–momentum dispersions parallel to the k_x direction are shown in Fig. 2c,g, k_y direction in Fig. 2d,e,h and k_z direction in Fig. 2f—these momentum cuts cover all high-symmetry points of the 3D Brillouin zone (namely, the Γ, X, W, K, L and U points).

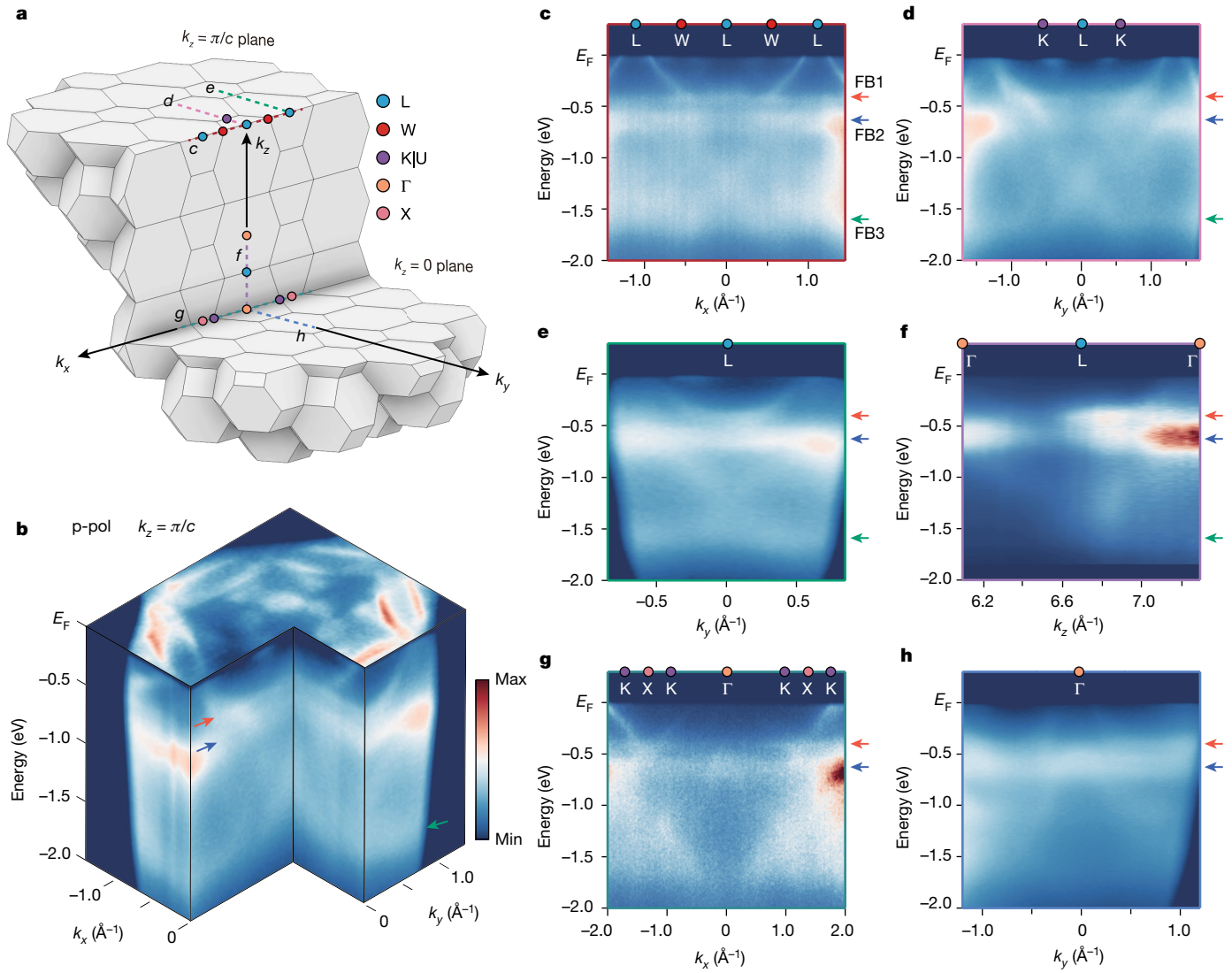

Fig. 2 | Pyrochlore flat bands in $CaNi_2$. **a**, Schematic of multiple three-dimensional Brillouin zones of $CaNi_2$. Filled circles represent the high-symmetry points. Coloured dashed lines mark the momentum directions of the ARPES data in **c**–**h**. **b**, Three-dimensional view of the electronic structure of $CaNi_2$ measured at the $k_z = \pi/c$ plane with linear horizontal polarization (p-pol). **c**–**h**, ARPES spectra along different momentum directions: **c**–**e** on the $k_z = \pi/c$ plane, **g**,**h** on the $k_z = 0$ plane and **f** along the k_z-axis (Γ–L–Γ). The red, blue and green arrows in **b**–**h** mark the energy positions of FB1, FB2 and FB3, respectively.

We observe several dispersive bands crossing the Fermi level, with well-defined Fermi surfaces (Fig. 2b) in accordance with the reported metallic behaviour[36]. We additionally identify three bands with significantly reduced dispersion at −0.41 ± 0.03 eV, −0.58 ± 0.03 eV and −1.58 ± 0.05 eV (Fig. 2, coloured arrows). In the following, we refer to these flat bands as FB1, FB2 and FB3, respectively. FB1 is flat along W–L, L–K and K–X (Fig. 2c,d,g) but becomes dispersive near Γ and crosses the Fermi level (Fig. 2f,g), precluding a direct estimation of its bandwidth. FB2 exhibits negligible dispersion across all high-symmetry points. Accounting for the experimental resolution and intrinsic broadening of the spectral function, we estimate the FB2 experimental bandwidth as $W_{FB2} \lesssim 80$ meV. This is more than an order of magnitude smaller than the observed dispersive bands. We estimate the FB3 experimental bandwidth as $W_{FB3} \lesssim 250$ meV; this is quenched relative to the dispersive bands, but also includes intrinsically dispersive regions (that is, near the L point; Fig. 2c–e). Overall, the observed flatness of FB1, FB2 and FB3 recalls that expected of the pyrochlore tight-binding model (Fig. 1g). In addition to these features, we observe the Dirac dispersion at W and quadratic-band touching point at Γ (Extended Data Fig. 3), also predicted for the pyrochlore network. All these spectroscopic features demonstrate the prototypical band structure of a pyrochlore metal in $CaNi_2$.

To verify the bulk origin of the observed flat bands, in Fig. 3d, we compare the momentum-integrated ARPES spectra (a proxy for density of states (DOS) if photoemission matrix elements are neglected) obtained using VUV and soft X-ray ARPES measurements on $CaNi_2$. The peaks in the experimental spectra are consistent across the VUV and soft X-ray ARPES data, supporting the bulk origin of the flat bands. We further compare the energy-distribution curves (EDCs) to the DFT-calculated DOS in Fig. 3d, identifying features at FB1 at −0.4 eV (shoulder), FB2 at −0.58 eV (sharp peak) and FB3 at −1.6 eV (broad hump). We further investigated the Fermi surface by measuring de Haas–van Alphen oscillations at low temperatures and high magnetic fields. These are consistent with the Fermi surface calculated from DFT with the same renormalization factor used for comparison with ARPES (a shift of 24 meV and scaling by 0.8; Methods and Supplementary Information section IV). The consistency of the quantum oscillation, DFT and ARPES results substantiate that the observed spectra are of bulk origin.

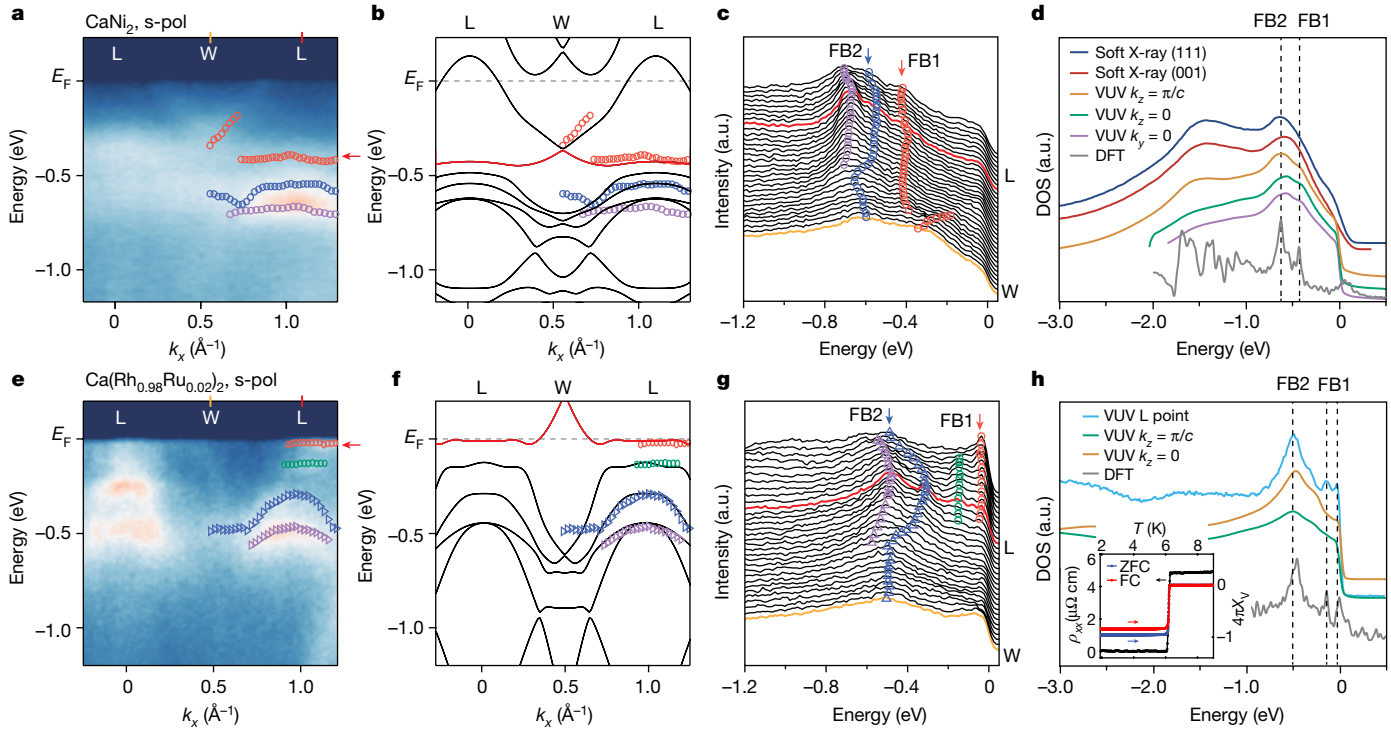

Fig. 3 | Tuning the pyrochlore flat bands towards the Fermi level. a,**b**, ARPES spectrum and DFT band structure of $CaNi_2$ along the L–W–L high-symmetry direction measured with linear vertical photon polarization (s-pol). The red arrow in **a** marks the energy position and the line in **b** marks the dispersion of FB1. **c**, EDCs along the momentum directions of **a**. The red and blue circles track the dispersions of FB1 and FB2, respectively. These EDC-extracted dispersions are also overlaid in **a**,**b** for comparison. a.u. denotes arbitrary units. **d**, ARPES spectra of $CaNi_2$ integrated over the given momentum ranges. The blue and red curves were integrated over the k_x–k_y planes corresponding to the (111) and (001) surfaces, respectively, using 500-eV soft X-ray photons. The orange, green and purple curves represent the momentum-integrated ARPES spectra collected by VUV photons at the $k_z = \pi/c$, $k_z = 0$ and $k_y = 0$ planes, respectively. The grey curve shows the DOS from DFT. Curves are offset for clarity; the vertical black dashed lines indicate the energies of the flat bands. **e**–**h**, Corresponding ARPES spectrum, DFT band structure, EDC stacks and integrated spectra for $Ca(Rh_{0.98}Ru_{0.02})_2$. The blue curve in **h** is the EDC extracted at the L point, whereas the orange and green curves are integrated over the $k_z = \pi/c$ and $k_z = 0$ planes, respectively. The inset of **h** shows superconductivity in $Ca(Rh_{0.98}Ru_{0.02})_2$ in resistivity and magnetic susceptibility measured at 5 Oe in both zero-field-cooled (ZFC) and field-cooled (FC) configurations.

Tuning the flat band to the Fermi level

The flat bands in $CaNi_2$ are located well below E_F, making them detectable by ARPES, but tempering possible effects on low-energy properties such as thermodynamics and transport quantities. The ability to push the flat bands closer to E_F such that one is partially filled would open the possibility of realizing instabilities towards symmetry breaking and exotic phases as noted in earlier theoretical studies[26,28,37]. To investigate the tunability of the pyrochlore flat bands, we synthesized single crystals of the isostructural C15 Laves phase $Ca(Rh_{1-x}Ru_x)_2$. In terms of electron count, replacing Ni with Rh and further adding Ru is expected to push the flat band towards the Fermi level while also introducing an enhanced bandwidth and spin–orbit coupling from the 4*d* orbitals.

Figure 3 compares the electronic structures of $CaNi_2$ and $Ca(Rh_{0.98}Ru_{0.02})_2$. Similar to $CaNi_2$, the ARPES spectra of $Ca(Rh_{0.98}Ru_{0.02})_2$ display a flat dispersion centred at −0.50 ± 0.1 eV, which manifests as a sharp peak in the integrated EDCs (Fig. 3h). Direct comparison between the $CaNi_2$ and $CaRh_2$ DFT band structures (the latter is used here given the DFT analysis suggests deviations of less than 10 meV for 2% doping; Supplementary Information section IV) reveals that this flat band corresponds to FB2 in $CaNi_2$ (Fig. 3b,f). We observe an additional flat dispersion at E_F (Fig. 3e, red arrow). This flat dispersion is visible below E_F near the L point, indicating its partially filled nature (see also EDCs in Fig. 3g,h). Orbital analysis of DFT shows that this flat band has the same character as FB1 in $CaNi_2$, but here it is split into two flat states: one at E_F and the other at −0.15 ± 0.05 eV (Fig. 3g, red and green circles, respectively), owing to the large spin–orbit splitting (see also Methods). Overall, strengthened spin–orbit gaps, hole doping and increased bandwidth from the more extended 4*d* electrons underpin this evolution and suggest material design approaches for ideal flat-band states.

In terms of physical properties, we observe a marked increase in the experimental Sommerfeld coefficient γ from 16.1 mJ mol^{-1} K^{-2} for $CaNi_2$ to 28.8 mJ mol^{-1} K^{-2} for $Ca(Rh_{0.98}Ru_{0.02})_2$ (Supplementary Information section I). Moreover, the coefficient measured for $Ca(Rh_{0.98}Ru_{0.02})_2$ is approximately 2.2 times larger than that calculated by DFT, larger than the ratio 1.8 observed for $CaNi_2$ (similar mass enhancements are observed in our quantum oscillation measurements; Methods). We also observe an increase in the Kadowaki–Woods ratio R_{KW} from 0.93 μΩ cm mol^2 K^2 J^{-2} in $CaNi_2$ to 2.53 μΩ cm mol^2 K^2 J^{-2} in $Ca(Rh_{0.98}Ru_{0.02})_2$ indicating an increase in electronic correlations (Supplementary Information section III). As reported in polycrystalline $CaRh_2$ (ref. 38), we find here that single crystals of $Ca(Rh_{1-x}Ru_x)_2$ are superconductors with transition temperatures as large as $T_C = 6.2$ K (Fig. 3h, inset). An important prospect is that further tuning and study of these structures may shed light on the interplay of electronic correlation, electron–phonon coupling and flat-band states[39] in the emergent properties of this materials family. These observations validate the notion that the pyrochlore flat bands can be tuned to E_F using control of electron filling, bandwidth and spin–orbit coupling strength in C15 Laves phase materials.

Electronic structure calculations

The DFT electronic structure and orbital-resolved DOS for $CaNi_2$ are shown in Fig. 4a. At the pyrochlore site, the d_{z^2} orbitals form an isotropic hopping network identical in symmetry to that of the single *s*-orbital pyrochlore model (Fig. 1g). In Fig. 4b, we compute the orbital projection

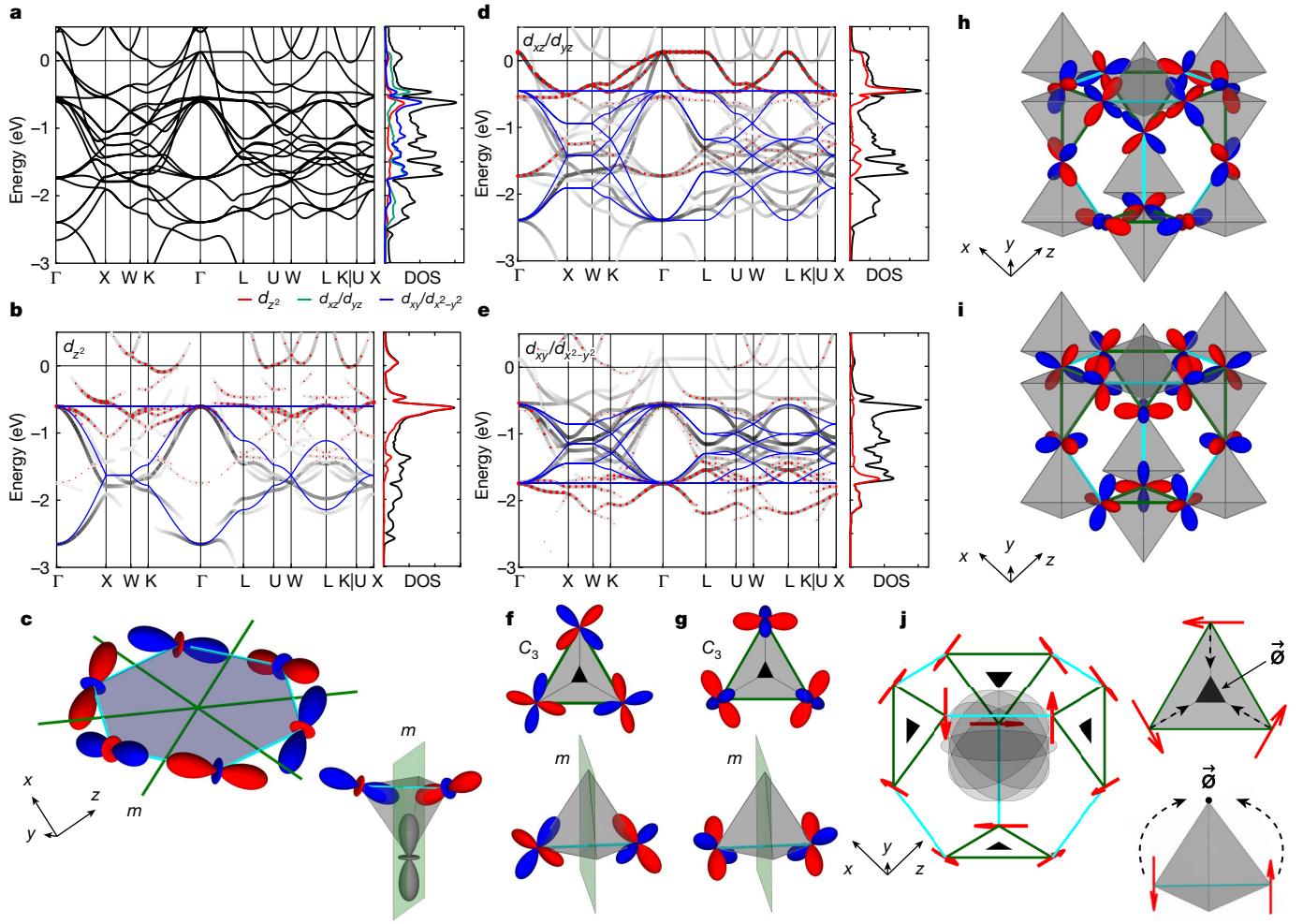

Fig. 4 | $CaNi_2$ electronic structure and flat bands. a, DFT band structure and the orbital-resolved DOS. Calculations are renormalized as described in the text. **b**, Local Ni d_{z^2} orbital projections (black lines). The blue lines denote the *s*-orbital pyrochlore model and the sizes of the red circles represent the Ni d_{z^2} flat-band weight projected from the DFT bands. **c**, Hexagonal plaquette CLS for the Ni d_{z^2} pyrochlore model. The orbital arrangement and mirror cancellation on a tetrahedron are shown on the right. The axes shown here and in **h**–**j** are the global cubic system axes in agreement with Fig. 1; the local axes at each site along which the orbitals are oriented are defined in Supplementary Information section V. **d**,**e**, Local Ni d_{xz}/d_{yz} (**d**) and $d_{xy}/d_{x^2-y^2}$ (**e**) orbital projections (black), with the simplified eight-band tight-binding model (blue). The d_{xz}/d_{yz} and $d_{xy}/d_{x^2-y^2}$ flat-band projection weights are shown as red circles. **f**,**g**, The three-site (top) and two-site (bottom) cancellation mechanism from the quantum interference in the d_{xz}/d_{yz} model (**f**) and the $d_{xy}/d_{x^2-y^2}$ model (**g**). **h**,**i**, 3D CLS for the d_{xz}/d_{yz} (**h**), and $d_{xy}/d_{x^2-y^2}$ (**i**) pyrochlore models. **j**, 3D CLS derived from simplified *x*/*y* vector models. The localized state is stabilized in a truncated tetrahedron, with the relevant C_3 rotation and mirror symmetries shown acting on the 3D CLS. The tetrahedra on the right side show the vector destructive interference ($\vec{\emptyset}$).

of the d_{z^2} bands within the electronic structure of $CaNi_2$ (black line) and find that DFT reproduces the flat and dispersive band features of the isotropic pyrochlore model (thin blue line). This d_{z^2} flat-band energy is consistent with FB2 in ARPES (Fig. 2). Projecting the d_{z^2} DOS onto the subspace formed by the flat band CLS shows both the band character and d_{z^2} DOS peak are well described by the flat-band model (Fig. 4b, red dotted line). We, therefore, identify FB2 as originating from the frustration-driven CLS of the pyrochlore band structure at an isotropic tight-binding level. Figure 4c shows such a CLS made from d_{z^2} orbitals encircling a hexagonal plaquette on which any two d_{z^2} orbitals sharing a tetrahedron destructively interfere (Fig. 4c, right side).

The above single-orbital isotropic tight-binding description is inadequate to capture FB1 and FB3—instead we consider their origin in the d_{xz}/d_{yz} and $d_{xy}/d_{x^2-y^2}$ orbital manifolds, respectively, which decorate the pyrochlore structure. In contrast with the d_{z^2} *s*-orbital-like hopping model, here the geometrical structure of hopping is derived from the 2D irreducible representation E_g at the pyrochlore sites with D_{3d} local symmetry. These can be viewed as a generalization from scalar *s*-orbitals to vector objects, with isotropic hopping promoted to matrix coupling (see Supplementary Information section V for further details). Referred to here as an *x*/*y* pyrochlore model, these support 3D destructive interference that quenches kinetic energy, yielding flat 3D doubly-degenerate bands for certain symmetry constraints (see below). In Fig. 4d,e, we compare the orbitally projected bands (black lines), with their overlap with the *x*/*y* CLS manifold (red dotted lined), as well as the ideal flat-band tight-binding models (blue lines), for d_{xz}/d_{yz} and $d_{xy}/d_{x^2-y^2}$. The flat-band positions and weights compare reasonably with the observations for FB1 and FB3 from ARPES (Fig. 2).

Discussion

To elucidate the physical origin of these *x*/*y* orbital flat bands, we examine the associated minimal CLSs in Fig. 4h,i. We find that the CLSs extend in all three dimensions within the pyrochlore lattice. This can be contrasted with the minimal CLS of the d_{z^2} flat band that forms a 2D hexagonal plaquette normal to ⟨111⟩ (Fig. 4c). Compared with the

scalar *s*-orbital model, the interference here is vectorial in nature (that is, $\sum_i c_i \mathbf{d}_i = \mathbf{0}$, where c_i are complex numbers and $\mathbf{d}_i$ are the x/y orbitals), enabling additional formation mechanisms for CLSs. For example, as shown in Fig. 4f,g, three d_{xz}/d_{yz} (Fig. 4f, top) and $d_{xy}/d_{x^2-y^2}$ (Fig. 4g, top) states on corners of a single tetrahedron form a threefold rotationally symmetric combination. This is incompatible with any site symmetry on the remaining corner and quenches hopping (a related mechanism has been discussed for RCo_5 compounds[40]). In addition, adjacent d_{xz}/d_{yz} orbitals have an odd mirror symmetry and $d_{xy}/d_{x^2-y^2}$ orbitals have an even mirror symmetry for their bisecting plane m (Fig. 4f,g, bottom), which leads to hopping cancellation to orbitals with opposite mirror symmetry on neighbouring sites. While this weakens the electronic dispersion, other hopping channels may generally remain (see below and Supplementary Information section V). The ideal case realizes an extended 3D CLS in the form of a truncated tetrahedron, shown as an outlined structure in Fig. 4h,i.

To examine the general hopping within these vector interference states, we compute the Wannierization of the $CaNi_2$ band structure. Consistent with the observation of FB1 and FB3, we find that the effective tight-binding parameters are proximate to those required for the ideal flat band (Supplementary Information section Vb). Deviations therefrom manifest in, for example, the lifting of degeneracy of the flat band and the observed dispersion of FB1 near Γ and FB3 near L (see Fig. 2). This is particularly apparent for FB3 and suggests that the choice of the orbital plays a key role in determining the degree of ideality of such flat-band states. The observed deviations from flatness are comparable to those, for example, expected for the next-nearest-neighbour hopping and inter-orbital hybridization[19], suggesting that these are important in considering engineering emergent 3D CLSs and higher-dimensional flat-band materials. As shown in Fig. 4j, these vector interference flat bands appear to be stabilized in $CaNi_2$ by a combination of symmetry-enforced destructive interference and cancellation of *d*-orbital hopping on the pyrochlore tetrahedra, extending the notion of scalar cancellation on the kagome plane (Fig. 1a). We expect that these emergent flat-band states may be a hallmark of constructing flat bands on high-symmetry, 3D networks.

Perspective

Similar to kagome metals, in $CaNi_2$, the pyrochlore metal behaviour is admixed with other bands and the influence of spacer (here Ca) atoms that complicate the electronic structure. The band dispersion and large DOS observed herein are strong evidence for the significant band flattening that persists and point towards potential strong correlation effects that may be accessible with chemical and mechanical tuning of this material family. These flat bands present unique opportunities for mixing electronic correlation and topology given their origin as CLSs[17], offering potential pathways to realizing unusual phases[15,16]. Further isolation of the flat band within the *d*-electron spectrum could potentially be achieved by identifying material structures with stronger crystal electric-field effects. At the same time, recent work has predicted that non-isolated flat bands may host unique correlated phenomena, including robust multi-band[26] and chiral[13] superconductivity and may further enable Kondo behaviour observed in other *d*-electron flat-band systems[30]. These examples suggest that a broad array of exotica may potentially be enabled within this platform.

Online content

Any methods, additional references, Nature Portfolio reporting summaries, source data, extended data, supplementary information, acknowledgements, peer review information; details of author contributions and competing interests; and statements of data and code availability are available at https://doi.org/10.1038/s41586-023-06640-1.

1. Liu, Z., Liu, F. & Wu, Y.-S. Exotic electronic states in the world of flat bands: from theory to material. *Chin. Phys. B* **23**, 077308 (2014).
2. Lieb, E. H. Two theorems on the Hubbard model. *Phys. Rev. Lett.* **62**, 1201–1204 (1989).
3. Sheng, D. N., Gu, Z.-C., Sun, K. & Sheng, L. Fractional quantum Hall effect in the absence of Landau levels. *Nat. Commun.* **2**, 389 (2011).
4. Regnault, N. & Bernevig, B. A. Fractional Chern insulator. *Phys. Rev. X* **1**, 021014 (2011).
5. Cao, Y. et al. Unconventional superconductivity in magic-angle graphene superlattices. *Nature* **556**, 43–50 (2018).
6. Mao, J. et al. Evidence of flat bands and correlated states in buckled graphene superlattices. *Nature* **584**, 215–220 (2020).
7. Li, Z. et al. Realization of flat band with possible nontrivial topology in electronic Kagome lattice. *Sci. Adv.* **4**, eaau4511 (2018).
8. Kang, M. et al. Dirac fermions and flat bands in the ideal kagome metal FeSn. *Nat. Mater.* **19**, 163–169 (2020).
9. Nishino, S. & Goda, M. Three-dimensional flat-band models. *J. Phys. Soc. Jpn.* **74**, 393–400 (2005).
10. Regnault, N. et al. Catalogue of flat-band stoichiometric materials. *Nature* **603**, 824–828 (2022).
11. Weeks, C. & Franz, M. Flat bands with nontrivial topology in three dimensions. *Phys. Rev. B* **85**, 041104 (2012).
12. Zhou, Y., Jin, K.-H., Huang, H., Wang, Z. & Liu, F. Weyl points created by a three-dimensional flat band. *Phys. Rev. B* **99**, 201105 (2019).
13. Lin, Y.-P. Chiral flat band superconductivity from symmetry-protected three-band crossings. *Phys. Rev. Res.* **2**, 043209 (2020).
14. Pesin, D. & Balents, L. Mott physics and band topology in materials with strong spin–orbit interaction. *Nat. Phys.* **6**, 376–381 (2010).
15. Guo, H.-M. & Franz, M. Three-dimensional topological insulators on the pyrochlore lattice. *Phys. Rev. Lett.* **103**, 206805 (2009).
16. Maciejko, J. & Fiete, G. A. Fractionalized topological insulators. *Nat. Phys.* **11**, 385–388 (2015).
17. Bergman, D. L., Wu, C. & Balents, L. Band touching from real-space topology in frustrated hopping models. *Phys. Rev. B* **78**, 125104 (2008).
18. Wu, C., Bergman, D., Balents, L. & Das Sarma, S. Flat bands and Wigner crystallization in the honeycomb optical lattice. *Phys. Rev. Lett.* **99**, 070401 (2007).
19. Kang, M. et al. Topological flat bands in frustrated kagome lattice CoSn. *Nat. Commun.* **11**, 4004 (2020).
20. Liu, Z. et al. Orbital-selective Dirac fermions and extremely flat bands in frustrated kagome-lattice metal CoSn. *Nat. Commun.* **11**, 4002 (2020).
21. Li, M. et al. Dirac cone, flat band and saddle point in kagome magnet YMn_6Sn_6. *Nat. Commun.* **12**, 3129 (2021).
22. Mielke, A. Ferromagnetic ground states for the Hubbard model on line graphs. *J. Phys. A Math. Gen.* **24**, L73–L77 (1991).
23. Lin, Z. et al. Flatbands and emergent ferromagnetic ordering in Fe_3Sn_2 kagome lattices. *Phys. Rev. Lett.* **121**, 096401 (2018).
24. Yin, J.-X. et al. Negative flat band magnetism in a spin–orbit-coupled correlated kagome magnet. *Nat. Phys.* **15**, 443–448 (2019).
25. Guo, H.-M. & Franz, M. Topological insulator on the kagome lattice. *Phys. Rev. B* **80**, 113102 (2009).
26. Aoki, H. Theoretical possibilities for flat band superconductivity. *J. Supercond. Nov. Magn.* **33**, 2341–2346 (2020).
27. Jiang, W., de Sousa, D. J. P., Wang, J.-P. & Low, T. Giant anomalous Hall effect due to double-degenerate quasiflat bands. *Phys. Rev. Lett.* **126**, 106601 (2021).
28. Trescher, M. & Bergholtz, E. J. Flat bands with higher Chern number in pyrochlore slabs. *Phys. Rev. B* **86**, 241111 (2012).
29. Wohlfarth, E. P. Very weak itinerant ferromagnets; application to $ZrZn_2$. *J. Appl. Phys.* **39**, 1061–1066 (1968).
30. Kondo, S. et al. LiV_2O_4: a heavy fermion transition metal oxide. *Phys. Rev. Lett.* **78**, 3729–3732 (1997).
31. Tian, Z. et al. Field-induced quantum metal–insulator transition in the pyrochlore iridate $Nd_2Ir_2O_7$. *Nat. Phys.* **12**, 134–138 (2016).
32. Wan, X., Turner, A. M., Vishwanath, A. & Savrasov, S. Y. Topological semimetal and Fermi-arc surface states in the electronic structure of pyrochlore iridates. *Phys. Rev. B* **83**, 205101 (2011).
33. Kondo, T. et al. Quadratic Fermi node in a 3D strongly correlated semimetal. *Nat. Commun.* **6**, 10042 (2015).
34. Sakai, H. et al. Superconductivity in a pyrochlore oxide, $Cd_2Re_2O_7$. *J. Phys. Condens. Matter* **13**, L785 (2001).
35. Hiroi, Z., Yonezawa, S. & Muraoka, Y. Unprecedented superconductivity in β-pyrochlore osmate KOs_2O_6. *J. Phys. Soc. Jpn.* **73**, 1651–1654 (2004).
36. Jesche, A., Dennis, K. W., Kreyssig, A. & Canfield, P. C. Nearly itinerant ferromagnetism in $CaNi_2$ and $CaNi_3$. *Phys. Rev. B* **85**, 224432 (2012).
37. Tang, E., Mei, J.-W. & Wen, X.-G. High-temperature fractional quantum Hall states. *Phys. Rev. Lett.* **106**, 236802 (2011).
38. Matthias, B. T. & Corenzwit, E. Superconducting alkaline earth compounds. *Phys. Rev.* **107**, 1558 (1957).
39. Ojajärvi, R., Hyart, T., Silaev, M. A. & Heikkilä, T. T. Competition of electron-phonon mediated superconductivity and Stoner magnetism on a flat band. *Phys. Rev. B* **98**, 054515 (2018).
40. Ochi, M., Arita, R., Matsumoto, M., Kino, H. & Miyake, T. Robust flat bands in RCo_5 (R=rare earth) compounds. *Phys. Rev. B* **91**, 165137 (2015).

Methods

Single-crystal growth

Single crystals of $CaNi_2$ and $Ca(Rh_{1-x}Ru_x)_2$ (space group $Fd\bar{3}m$) were grown using a Ca self-flux method in line with a previous report[36] (previously, only synthesis of polycrystalline $CaRh_2$ has been reported[38,41]). For growth of $CaNi_2$, Ca (99.98%) and Ni (99.99%) were mixed in a molar ratio of 2:1 and placed inside a Ta crucible. A Ta strainer was placed above the elements, and the crucible was sealed under Ar atmosphere by arc melting and further sealed inside a quartz tube. The tube was heated to 1,050 °C, held for 1 day, cooled to 900 °C over 2 days and cooled further to 650 °C over 8 days. Finally, the material was annealed at 650 °C for 2 days before decanting. Single crystals of $Ca(Rh_{1-x}Ru_x)_2$ were grown from a mixture of Ca (99.98%), Rh (99.95%) and Ru (99.99%) in a molar ratio of Ca:(Rh,Ru) = 3:2. The elements were placed in an alumina crucible, sealed under vacuum and heated to 1,020 °C before being cooled over 1 week to 520 °C, held for 48 h and finally cooled to room temperature.

Crystallization occurred primarily in the octahedral morphology typical for materials of a cubic space group in which the triangular faces identify the (111) crystallographic planes (Supplementary Fig. 1, inset). The typical crystal size was approximately $1 \times 1 \times 1\ mm^3$ for $CaNi_2$ and $0.3 \times 0.3 \times 0.3\ mm^3$ for $Ca(Rh_{1-x}Ru_x)_2$. The crystals were characterized with powder X-ray diffraction and agreed with the reported structure. $Ca(Rh_{1-x}Ru_x)_2$ crystals were additionally characterized with energy-dispersive X-ray spectroscopy that confirmed the final stoichiometry of the material. Single crystals of the composition $Ca(Rh_{0.98}Ru_{0.02})_2$ (grown from an initial molar ratio of Ca:Rh:Ru = 15:9:1) exhibited a higher crystal quality than undoped $CaRh_2$.

ARPES

VUV-ARPES experiments were performed at Beamline 7.0.2 (MAESTRO) of the Advanced Light Source and Beamline 21-ID-1 (ESM) of the National Synchrotron Light Source II equipped with R4000 and DA30 hemispherical electron analysers (Scienta Omicron), respectively. Crystals were cleaved parallel to the (111) plane in an ultra-high vacuum chamber with a base pressure lower than 4×10^{-11} Torr. In 3D materials such as pyrochlore systems, the spatial inhomogeneity of the cleaved surface often hinders the acquisition of a clear ARPES spectrum. We overcome this issue by using micro-focused synchrotron radiation with a beam spot smaller than $20 \times 30\ \mu m^2$ and by identifying partially flat-surface regions on otherwise rough cleaved surfaces.

To identify the high-symmetry points along the out-of-plane momentum k_z, the photon energy was scanned from 80 eV to 200 eV at the MAESTRO beamline and from 175 eV to 370 eV at the ESM beamline, spanning more than three complete 3D Brillouin zones. The k_z value is estimated using the standard nearly-free-electron final-state approximation with inner potential $V_0 = 5$ eV. The ARPES spectra along various high-symmetry directions were obtained by collecting photoelectrons from three principal momentum planes in the 3D momentum–space: the k_x–k_y plane at $k_z = 0$, the k_x–k_y plane at $k_z = \pi/c$ and the k_x–k_z plane at $k_y = 0$. The k_x–k_y planes were measured by electron deflector scans at fixed photon energies, whereas the k_x–k_z plane was obtained from the photon-energy scans. We estimate the momentum step size along the k_x, k_y and k_z directions as 0.010 $Å^{-1}$, 0.026 $Å^{-1}$ and 0.026 $Å^{-1}$, respectively. All datasets were collected at temperatures below 10 K and linear horizontal photon polarization unless otherwise specified. For 3D materials, background contributions may arise from k_z broadening effects and inhomogeneity of the cleaved surface, which is minimized here by optimization of spectral quality and beam spot size. Furthermore, FB3 is spectrally broadened, probably because of a decreased quasi-particle lifetime at higher binding energies.

Soft X-ray ARPES experiments were performed at beamline 29-ID of the Advanced Photon Source. Beamline 29-ID is equipped with a Scienta R4000 analyser. Data were taken at 50 K and 500 eV with circularly polarized light. Samples were cleaved in a vacuum chamber with a pressure lower than 6×10^{-10} Torr. Sample degradation was typically observed after approximately 8 h. Scans at different angles are normalized relative to the momentum-independent background below a binding energy of −3 eV. As described in the main text, the consistency in the VUV ARPES, soft X-ray ARPES, quantum oscillations and DFT calculations supports the intrinsic, bulk origin of the observed electronic structures. We further rule out extrinsic factors, such as defect scattering and k_z broadening, affecting the flat dispersions in the ARPES spectra.

The geometry of the VUV-ARPES experiments is shown in Extended Data Fig. 1a. The incident VUV photons are shown by a purple arrow, and the blue horizontal plane represents the photon incidence and electron emission plane, which is made to coincide with a mirror plane of the sample. To determine the value of k_z in $CaNi_2$, we simulated the photoelectron trajectory as a function of incident photon energy (Extended Data Fig. 1b). The red and green curves show the simulated trajectories of photoelectrons with steps of 5 eV. The green curves indicate the incident photon energies of 135 eV and 175 eV used to measure the energy–momentum dispersions at $k_z = 0$ and $k_z = \pi/c$, respectively. For $Ca(Rh_{0.98}Ru_{0.02})_2$, the 127-eV and 97-eV photons measure the $k_z = 0$ and $k_z = \pi/c$ planes, respectively. Extended Data Fig. 1c–e shows the truncated 3D Brillouin zones corresponding to the k_x–k_z plane at $k_y = 0$, k_x–k_y plane at $k_z = 0$ and k_x–k_y plane at $k_z = \pi/c$.

In Extended Data Fig. 2, we provide further analysis of the $CaNi_2$ flat-band dispersions using second-derivative plots and DFT. We also investigated additional momentum–space directions on the $k_z = -1/3 \times \pi/c$ plane. Extended Data Fig. 2a–d shows the schematic of the 3D Brillouin zones of $CaNi_2$. Brown, cyan, green and purple dashed lines mark the various momentum–space directions investigated in Extended Data Fig. 2e–p. Note that in Extended Data Fig. 2c,d, we defined additional momentum point Γ_1 for convenience, which is a projection of the Γ point to the $k_z = -1/3 \times \pi/c$ plane. Extended Data Fig. 2e–p shows the ARPES spectra, second-derivative plots and DFT band structures of $CaNi_2$ measured along the K–Γ–K (Extended Data Fig. 2e–g), K–Γ_1–L (Extended Data Fig. 2h–j), Γ–L–Γ (Extended Data Fig. 2k–m) and Γ_1–L–Γ_1 (Extended Data Fig. 2n–p) momentum directions. The dispersions of FB1 and FB2 are clear in the second-derivative plots of Extended Data Fig. 2f,l. This demonstrates that the dispersion of FB2 is quenched along both directions, whereas FB1 acquires some dispersion near Γ as discussed earlier. The DFT band structures in Extended Data Fig. 2g,m reproduce this behaviour. Meanwhile, the partial dispersion of FB3 can be seen in the second-derivative plots across Γ_1 (Extended Data Fig. 2i,o). The dispersion of FB3 is also captured by the DFT calculation (Extended Data Fig. 2j,p).

In the main text and above, we focused on the flat-band dispersions in the pyrochlore lattice. In Extended Data Figs. 3–5, we demonstrate our observations of other characteristic electronic structures of the pyrochlore lattice, including the quadratic-band touching point at Γ, Dirac nodes at W, gapless Dirac crossing at X and saddle-point dispersion at L.

Extended Data Fig. 3 shows the ARPES dispersions of $CaNi_2$. The black arrow in Extended Data Fig. 3a–c highlights the quadratic-band touching point at which the doubly-degenerate flat bands and the dispersive bands touch quadratically at the Γ point. Extended Data Fig. 3d–f presents the ARPES spectrum, second-derivative plot and DFT band structure, showing the Dirac nodes at the W points. Both of these are key constituents of the pyrochlore electronic structure (Fig. 1g). To illustrate the full 3D electronic structure of $CaNi_2$, we plot a series of ARPES spectra along high-symmetry directions in Extended Data Fig. 3h. This projected view highlights the quenched dispersion and flatness of FB2 along all three electron–momentum axes. The weak dispersive nature of FB1 and FB3 can be also identified.

Extended Data Fig. 4a,b shows the ARPES spectra of $Ca(Rh_{0.98}Ru_{0.02})_2$ and DFT band structure of $CaRh_2$ (used for comparison here given the

light chemical-doping calculations using a virtual crystal approximation indicate band deviations of less than 10 meV for $x = 0.02$; Supplementary Information section IV). As seen in $CaNi_2$ (Extended Data Fig. 3a–c), we observed the flat band and the dispersive bands coexisting near the Γ point. A close examination of the dispersions using the energy-distribution curves (Extended Data Fig. 4c) further revealed the lifting of the quadratic-band touching at Γ by the spin–orbit coupling (SOC) in $Ca(Rh_{0.98}Ru_{0.02})_2$, resulting in an SOC gap between the flat bands and the dispersive bands.

The SOC also lifts the line-nodal degeneracy along X–W (Fig. 1g). In this case, only the bands at the X point remain doubly degenerate, and a 3D Dirac crossing is realized at X. As shown in Extended Data Fig. 4d–f, this Dirac crossing is observed in the ARPES spectra, second-derivative plots and DFT of $Ca(Rh_{0.98}Ru_{0.02})_2$.

Finally, the tight-binding band structure of the pyrochlore lattice also exhibits several saddle-point dispersions that are reminiscent of the van Hove singularities in the 2D kagome lattice. In Extended Data Fig. 5, we demonstrate the saddle-point dispersion at L in $Ca(Rh_{0.98}Ru_{0.02})_2$. Extended Data Fig. 5a,b shows the experimental and calculated Fermi surfaces of $Ca(Rh_{0.98}Ru_{0.02})_2$ at $k_z = \pi/c$. Extended Data Fig. 5c,f shows the APRES spectra measured along the two perpendicular momentum directions crossing the L point as marked in Extended Data Fig. 5a. Near the binding energy of 0.15 eV, we observed the hole-like dispersion at L along the k_x direction (Extended Data Fig. 5c) and the electron-like dispersion along the k_y direction (Extended Data Fig. 5f). This provides direct evidence of the formation of a saddle point at L. The second-derivative plots in Extended Data Fig. 5d,g and the DFT calculations in Extended Data Fig. 5e,h further corroborate this observation.

Transport measurements

Longitudinal transport measurements were taken in a four-probe geometry for temperatures down to 1.8 K in a commercial cryostat. Measurements were taken with the current in the (111) plane. Data were collected using the standard a.c. technique with a lock-in amplifier using a typical current bias of 1–10 mA.

Magnetization measurements

Temperature-dependent magnetization measurements were taken using a vibrating-sample magnetometer for temperatures down to 1.9 K in a commercial cryostat. All data were demagnetization corrected[42]. Measurements were taken in a zero-field-cooled configuration as well as in a field-cooled environment.

de Haas–van Alphen quantum oscillations

To further probe the Fermi surfaces of $CaNi_2$ and $Ca(Rh_{0.98}Ru_{0.02})_2$, we performed torque magnetometry measurements at low temperature and high magnetic fields to map de Haas–van Alphen (dHvA) quantum oscillation frequencies. dHvA oscillations were observed in scans at low temperatures and at all field angles for both systems.

Torque magnetometry measurements were performed at Cell 9 and Cell 6 of the National High Magnetic Field Laboratory. Torque was measured using piezoresistive cantilevers (SCL SensorTech PRSA-L300) with an excitation amplitude of 20 mV. The quantum oscillations were analysed after subtracting a polynomial background by taking the fast Fourier transform (FFT) of the data as a function of the inverse fields in a fixed magnetic-field range. Owing to the rapidly oscillating magnetization, the signal in $CaNi_2$ is prone to magnetic interaction effects[43]; analysis herein is confined to fields below the onset of magnetic interaction.

$CaNi_2$

In Extended Data Fig. 6, we show the evolution of the observed quantum oscillation frequencies of $CaNi_2$ as a function of field-rotation angle in the [100], [111] and [011] directions. From the experimental data, we verify a 3D Fermi surface qualitatively consistent with the cubic crystal symmetries. Comparing with DFT calculations of the Fermi surface (see below), we identify five Fermi-surface pockets (referred to here as α, β, δ, γ and ω). These pockets vary in ellipticity—the lower frequency α and β branches show nearly isotropic extremal areas, whereas the δ pocket shows an anisotropic character with several external orbit branches originating from a single Fermi sheet (which we denote as δ_1, δ_2, δ_3 and δ_4). This shape is captured by the renormalized DFT (Extended Data Figs. 8 and 9 and Supplementary Information section IV) as denoted by the dashed lines in Extended Data Fig. 6 (we observe consistent results using a tunnel-diode oscillator technique, described below). The consistency of the quantum oscillation, DFT and ARPES results substantiate that the observed spectra are of bulk origin.

For the torque magnetometry measurements of $CaNi_2$, two samples (T1 and T2) were mounted on piezoresistive cantilevers in a He-3 cryostat, and the oscillations were observed for fields above 8 T. The background-subtracted data are presented as a function of field and angle in Extended Data Fig. 6a,b for samples T1 and T2, respectively. The corresponding FFTs are presented in Extended Data Fig. 6c,d and show reasonable consistency. The field angle θ is defined as shown in Extended Data Fig. 6e with $\theta = 0°$ corresponding to $\mathbf{B} \parallel [100]$. In the angle dependence of the FFTs shown in Extended Data Fig. 6f, we identify six branches, five of which show close agreement with those of the calculated α, β, δ_1, δ_2 and δ_4, extremal orbits (see below and Extended Data Fig. 8). We identify the sixth branch with the second harmonic of δ_2.

The temperature dependence and FFT amplitudes for sample T1 at $\theta = 63°$ are shown in Extended Data Fig. 6g,h. The temperature-dependent amplitudes of the FFT peaks are fit to the thermal damping factor predicted by Lifshitz–Kosevich theory $R_T^i \sim \frac{2\pi^2 k_B T m_i^*}{\hbar e B} \sinh^{-1}\left(\frac{2\pi^2 k_B T m_i^*}{\hbar e B}\right)$ for a pocket i with effective mass m_i^*. This fitting is shown in Extended Data Fig. 6i with the corresponding pocket-dependent effective mass parameters extracted as: $m_\alpha^* = (0.57 \pm 0.03)m_e$, $m_\beta^* = (0.89 \pm 0.06)m_e$, $m_{\delta 1}^* = (1.45 \pm 0.07)m_e$ and $m_{\delta 2}^* = (1.47 \pm 0.09)m_e$, where m_e is the free-electron mass. These values can be compared with the calculated effective mass values of the unrenormalized system (with the same offset of E_F), which are $m_\alpha = 0.35m_e$, $m_\beta = 0.62m_e$, $m_{\delta 1} = 0.97m_e$ and $m_{\delta 2} = 0.93m_e$ calculated with the SKEAF code at the corresponding field angles. The ratio of these masses gives the band-dependent renormalization factors of the system m_{dHvA}^*/m_{DFT} as 1.63, 1.44, 1.49 and 1.58 for α, β, δ_1 and δ_2, respectively.

$Ca(Rh_{0.98}Ru_{0.02})_2$

Torque magnetometry was performed on single crystals of $Ca(Rh_{0.98}Ru_{0.02})_2$ up to 41 T. In Extended Data Fig. 7a, we show the field-angle evolution of the observed frequencies with the sample geometry as defined in Extended Data Fig. 7d, in which $\theta = 0°$ corresponds to the [111] direction. Background-subtracted torque data are presented in Extended Data Fig. 7b with corresponding FFT amplitudes in Extended Data Fig. 7c. Similar to $CaNi_2$, a 3D Fermi surface is observed with reasonable agreement between the DFT calculated and observed frequencies. In the angle-dependent data, we observe two frequency branches near 4,000 T and 750 T that we identify with Fermi sheets α and δ, respectively, from the DFT Fermi-surface calculations (Extended Data Fig. 10 and Supplementary Information section IV). At He-3 temperatures, we observe signatures of a partial frequency branch near 1,000 T consistent with a pocket in the γ Fermi sheet; lower temperatures are probably needed to definitively resolve this. To extract the effective masses of the observed bands, we took temperature-dependent data at $\theta = 176°$ with the background-subtracted data and corresponding FFT amplitudes shown in Extended Data Fig. 7e,f. We resolved effective masses $m_\alpha^* = (0.82 \pm 0.02)m_e$ and $m_\delta^* = (1.62 \pm 0.09)m_e$ according to the Lifshitz–Kosevich temperature-dependent fit in Extended Data

Fig. 7g. We can compare these effective masses with those of the DFT calculations $m_\alpha = 0.45m_e$ and $m_\delta = 0.71m_e$ to obtain band-dependent renormalization factors m^*_{dHvA}/m_{DFT} of 1.82 for α and 2.28 for δ.

Tunnel-diode oscillator measurements

Tunnel-diode oscillator measurements were performed at Cell 9 of the National High Magnetic Field Laboratory. These measurements were taken with a crystal in the centre of an inductance coil of an LC circuit maintained at resonance[44]. A polynomial background is subtracted for quantum oscillation analysis, focusing on the field range 15–31.4 T.

Proximity-detector oscillator measurements

Proximity-detector oscillator measurements were performed up to 60 T in a pulsed-field magnet at the National High Magnetic Field Laboratory Pulsed Field Facility at Los Alamos National Laboratory. The crystal was placed at the centre of a counterwound pancake coil and measurements were obtained as described elsewhere[45].

Specific-heat measurements

Specific heat was measured in a commercial cryostat using the thermal relaxation technique. To extract the low-temperature fitting, data were taken down to 1.8 K and at fields up to 4 T.

DFT calculations

We performed the DFT calculations implemented in Vienna Ab initio Simulation Package code[46,47], with the projector augmented wave method[48] for the pseudo-potential formalism. The ground state for the primitive unit cell is converged with exchange-correlation energies parametrized by Perdew, Burke and Ernzerhof[49], a 520-eV cutoff energy for the plane-wave basis set and a 6 × 6 × 6 Monkhorst–Pack grid sampling[50] in the reciprocal space. To derive the Fermi-surface properties, we also use the calculations implemented in the Elk code (http://elk.sourceforge.net), a DFT code based on an all-electron full-potential linearized augmented plane wave method. The electronic ground state is converged with the local density approximation exchange-correlation functional[51], a reciprocal k-grid size of 30 × 30 × 30 and a muffin-tin radius $R_{MT} = 1.26$ Å. The angular momentum is expanded up to $L = 8$ for the augmented-plane wave functions, with a plane wave basis cutoff of $7R_{MT}^{-1}$ for the interstitial region. The calculations were performed with the inclusion of SOC and show good agreement with those implemented with the Vienna Ab initio Simulation Package code. The quantum oscillation frequencies with their angular dependence were computed using the SKEAF code[52] for extracting extremal orbits and are overlaid onto Extended Data Figs. 6f and 7a and Supplementary Fig. S3d.

Computationally, in $CaNi_2$ we identify five unique Fermi sheets that we refer to as α, β, γ, δ and ω (shown in Extended Data Fig. 8a–e in order of smallest to largest). Whereas α, β and γ are of nearly spherical character with some distortions centred at Γ, the δ and ω Fermi sheets are more anisotropic. In Extended Data Fig. 9, we compare the calculated Fermi surfaces at $k_z = 0$ and $k_z = \pi/c$ with the experimental Fermi surfaces obtained from the VUV ARPES measurements. At $k_z = \pi/c$ (Extended Data Fig. 9a), the experimental Fermi surface identifies electron pockets near K|U and elliptical hole pockets at L, which correspond to the ω and δ pockets in the calculation, respectively. At $k_z = 0$ (Extended Data Fig. 9b), the ω pocket evolves into a triangular shape near K|U. The close agreement between the ARPES and DFT Fermi surfaces highlights the bulk nature of the dispersions observed in ARPES. In Extended Data Fig. 8f–h, we show the anisotropic δ Fermi sheet and indicate the representative extremal orbits of the four smallest-area branches for a field aligned along a high-symmetry direction. We label these δ_1, δ_2, δ_3 and δ_4. We also compute the Fermi sheets of $CaRh_2$ that are shown in Extended Data Fig. 10 and labelled as α, β, γ and δ with the Fermi sheet γ corresponding to the manifold of FB1 at the Fermi level.

Data availability

The data presented in the main text of this article are available from the Harvard Dataverse[53]. All other data are available from the corresponding authors upon reasonable request.

Code availability

The codes used for the density functional theory and analytical calculations in this study are available from the corresponding authors upon reasonable request.

41. Górnicka, K., Cava, R. J. & Klimczuk, T. The electronic characterization of the cubic Laves-phase superconductor $CaRh_2$. *J. Alloys Compd.* **793**, 393–399 (2019).
42. Joseph, R. I. Ballistic demagnetizing factor in uniformly magnetized rectangular prisms. *J. Appl. Phys.* **38**, 2405–2406 (1967).
43. Shoenberg, D. *Magnetic Oscillations in Metals* (Cambridge Univ. Press, 1984).
44. Athas, G. J., Brooks, J. S., Klepper, S. J., Uji, S. & Tokumoto, M. Tunnel diode oscillator application to high sensitivity de Haas–van Alphen and superconducting critical field studies of anisotropic organic conductors. *Rev. Sci. Instrum.* **64**, 3248–3251 (1993).
45. Altarawneh, M. M., Mielke, C. H. & Brooks, J. S. Proximity detector circuits: an alternative to tunnel diode oscillators for contactless measurements in pulsed magnetic field environments. *Rev. Sci. Instrum.* **80**, 066104 (2009).
46. Kresse, G. & Furthmüller, J. Efficient iterative schemes for *ab initio* total-energy calculations using a plane-wave basis set. *Phys. Rev. B* **54**, 11169–11186 (1996).
47. Kresse, G. & Furthmüller, J. Efficiency of ab-initio total energy calculations for metals and semiconductors using a plane-wave basis set. *Compt. Mater. Sci.* **6**, 15–50 (1996).
48. Blöchl, P. E. Projector augmented-wave method. *Phys. Rev. B* **50**, 17953–17979 (1994).
49. Perdew, J. P., Burke, K. & Ernzerhof, M. Generalized gradient approximation made simple. *Phys. Rev. Lett.* **77**, 3865–3868 (1996).
50. Monkhorst, H. J. & Pack, J. D. Special points for Brillouin-zone integrations. *Phys. Rev. B* **13**, 5188–5192 (1976).
51. Perdew, J. P. & Wang, Y. Accurate and simple analytic representation of the electron-gas correlation energy. *Phys. Rev. B* **45**, 13244–13249 (1992).
52. Rourke, P. M. C. & Julian, S. R. Numerical extraction of de Haas–van Alphen frequencies from calculated band energies. *Compt. Mater. Sci.* **183**, 324–332 (2012).
53. Wakefield, J. Replication data for: three dimensional flat bands in pyrochlore metal $CaNi_2$. Harvard Dataverse https://doi.org/10.7910/DVN/PB3HCI (2023).
54. Reuther, A. et al. Interactive supercomputing on 40,000 cores for machine learning and data analysis. In *2018 IEEE High Performance Extreme Computing Conference* (HPEC) 1–6 (IEEE, 2018).

Acknowledgements We appreciate the discussions with J. Cano and J. Singleton. This work was funded, in part, by the Gordon and Betty Moore Foundation EPiQS Initiative (grant no. GBMF9070 to J.G.C.) (instrumentation development, DFT calculations), the Air Force Office of Scientific Research (AFOSR) (award FA9550-22-1-0432) (material synthesis, ARPES) and the NSF (DMR-2104964) (material analysis) and the Center for Advancement of Topological Semimetals, an Energy Frontier Research Center funded by the US Department of Energy (DOE), Office of Science, Basic Energy Sciences (BES), through the Ames Laboratory (contract no. DE-AC02-07CH11358) (pulsed-field experiments). P.M.N. acknowledges support from the STC Center for Integrated Quantum Materials (NSF grant DMR-1231319). M.K., S.L., S.P. and J.-H.P. acknowledge support from the National Research Foundation of Korea (NRF) funded by the Ministry of Science and ICT (nos 2022M3H4A1A04074153 and 2020M3H4A2084417). M.L. acknowledges support from the DOE, BES (DE-SC0020148). T.S. acknowledges support from JSPS KAKENHI (grant no. 21K03454). This research used resources of the Advanced Light Source, which is a DOE, Office of Science, user facility (contract no. DE-AC02-05CH11231). This research used resources from the Advanced Photon Source, a DOE, Office of Science, user facility operated for the DOE, Office of Science, by the Argonne National Laboratory (contract no. DE-AC02-06CH11357). A portion of this work was performed at the National High Magnetic Field Laboratory, which is supported by the National Science Foundation Cooperative Agreement no. DMR-1644779, the State of Florida and the DOE. We thank the MIT SuperCloud[54] and the Lincoln Laboratory Supercomputing Center for providing high-performance computing resources that have contributed to the results reported in this study.

Author contributions J.P.W., P.M.N. and R.M. synthesized the materials with support from T.N.L., T.S. and M.L.; J.P.W. and P.M.N. characterized the materials; M.K., D.O., J.P.W. and P.M.N. performed and analysed VUV ARPES experiments with support from A.C., S.L., S.P., J.-H.P., C.J., A.B., E.R., A.R. and E.V.; J.P.W., P.M.N. and R.M. performed and analysed soft X-ray ARPES with support from J.L.M.; J.P.W. and P.M.N. performed and analysed quantum oscillation experiments with support from S.Y.F.Z., A.C., D.G. and J.C.P; S.F. performed DFT calculations; and J.P.W., P.M.N., S.F. and T.S. performed electronic and structural modelling and analysis. All authors contributed to writing the paper. R.C. and J.G.C. coordinated the project.

Competing interests The authors declare no competing interests.

Additional information

Supplementary information The online version contains supplementary material available at https://doi.org/10.1038/s41586-023-06640-1.

Correspondence and requests for materials should be addressed to Riccardo Comin or Joseph G. Checkelsky.

Peer review information *Nature* thanks Xingjiang Zhou and the other, anonymous, reviewer(s) for their contribution to the peer review of this work.

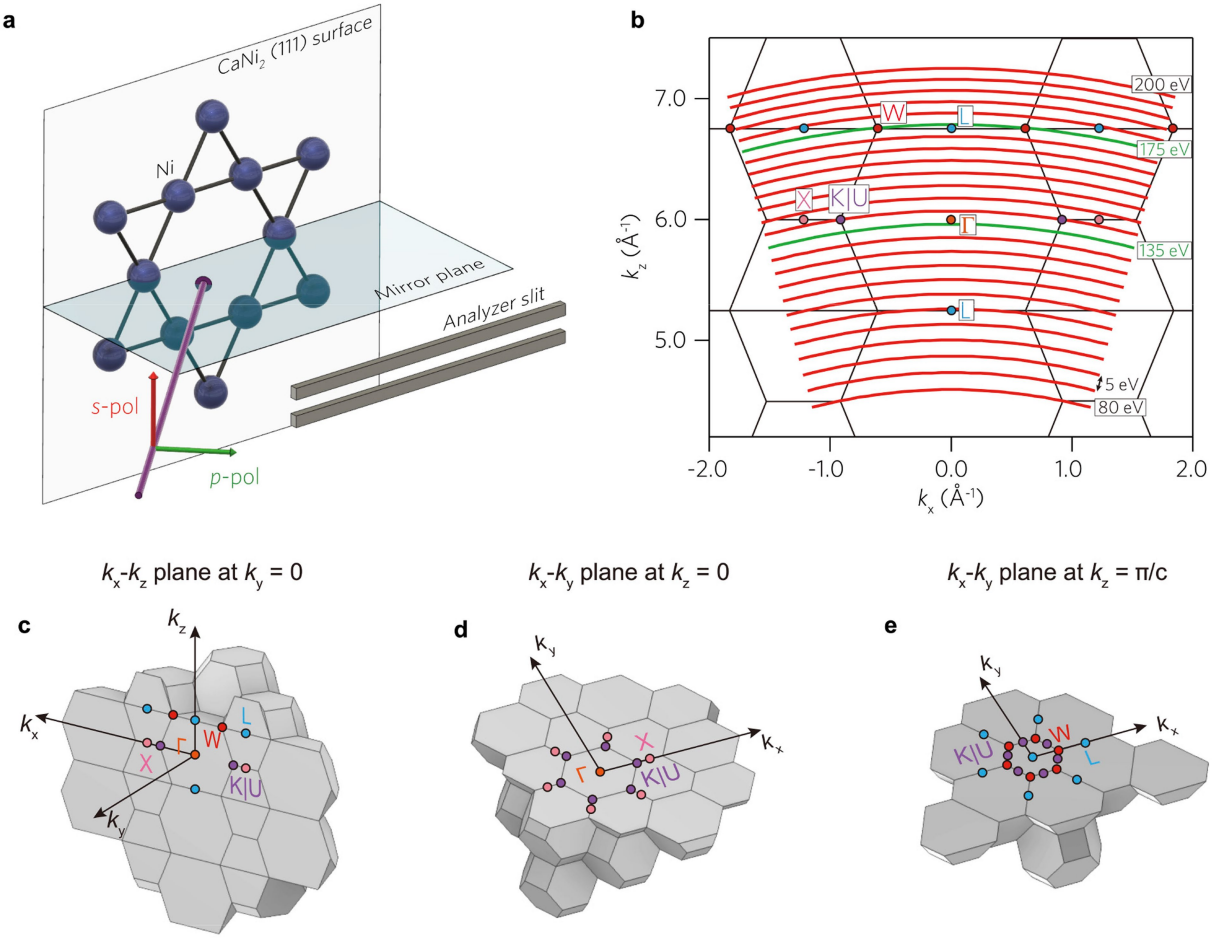

Extended Data Fig. 1 | Experimental setup of VUV-ARPES. (a) Experimental geometry of VUV-ARPES. (b) The simulated trajectory of photoelectrons for the photon energy-dependent ARPES experiment. Photoelectron trajectories from 80 eV to 200 eV were plotted as red and green curves with 5 eV steps. Black solid lines correspond to the bulk Brillouin zones. 3D Brillouin zones truncated by (c) k_x-k_z plane at $k_y = 0$, (d) k_x-k_y plane at $k_z = 0$, and (e) k_x-k_y plane at $k_z = \pi/c$.

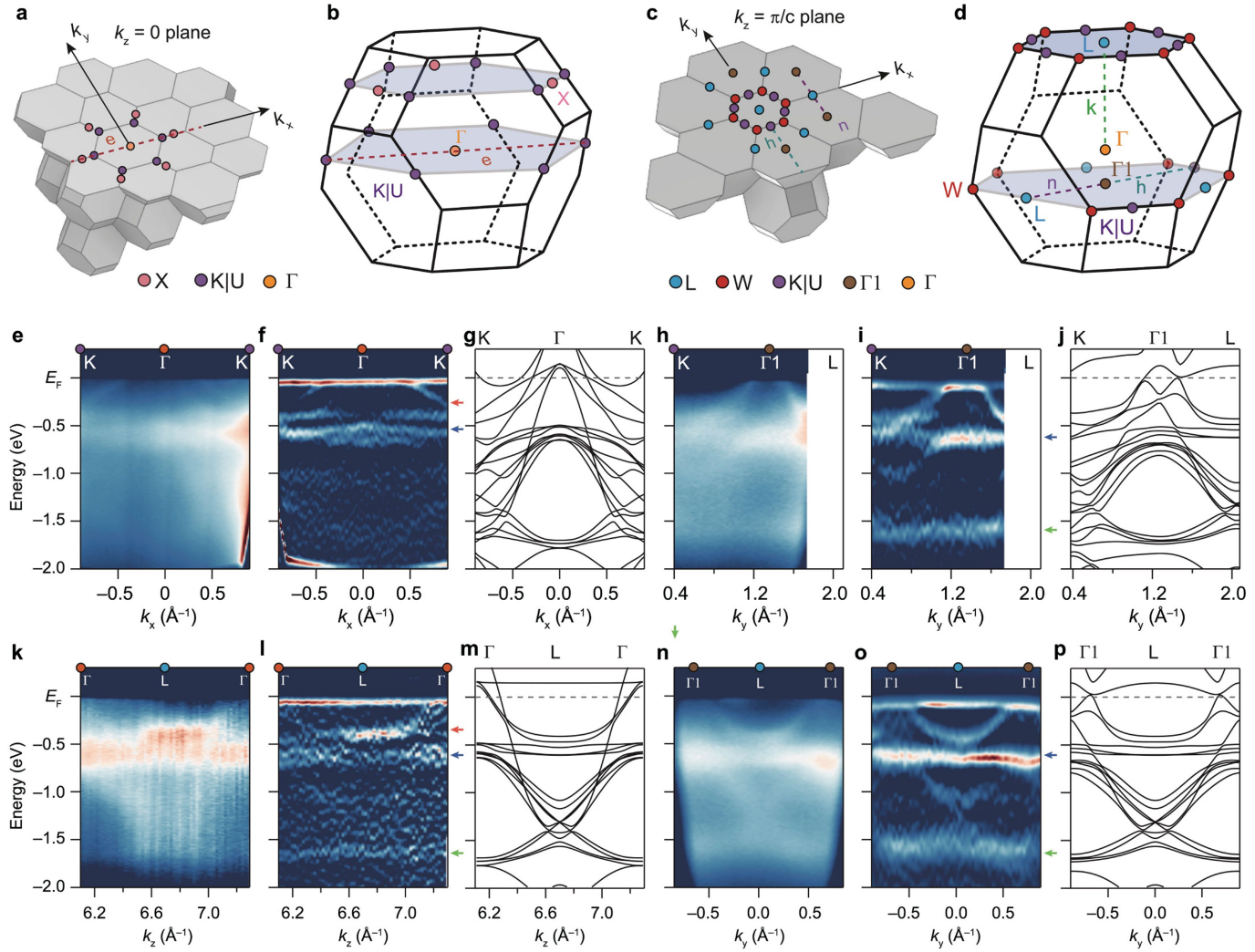

Extended Data Fig. 2 | Additional analysis of the flat bands in $CaNi_2$. (a) Schematics of the 3D Brillouin zones truncated by $k_z = 0$ plane of the first Brillouin zone. The truncation exposes the $k_z = 0$ plane of the first Brillouin zone and the $k_z = 2/3 \times \pi/c$ plane of the second Brillouin zones as marked with blue areas in (b). (c) Schematics of the 3D Brillouin zones truncated by $k_z = \pi/c$ plane of the first Brillouin zone. The truncation exposes the $k_z = \pi/c$ plane of the first Brillouin zone and the $k_z = -1/3 \times \pi/c$ plane of the second Brillouin zones as marked with blue areas in (d). In (c),(d), we defined a new momentum point Γ_1 as the projection of Γ to the $k_z = -1/3 \times \pi/c$ plane. (e),(h),(k),(n) ARPES spectra of $CaNi_2$ measured along the momentum directions marked with dashed-lines in (a-d). The corresponding second derivative plots and DFT band structures are shown in (f),(i),(l),(o) and (g),(j),(m),(p), respectively. The red, blue, and green arrows in (f),(i),(l),(o) mark the positions of FB1, FB2, and FB3, respectively.

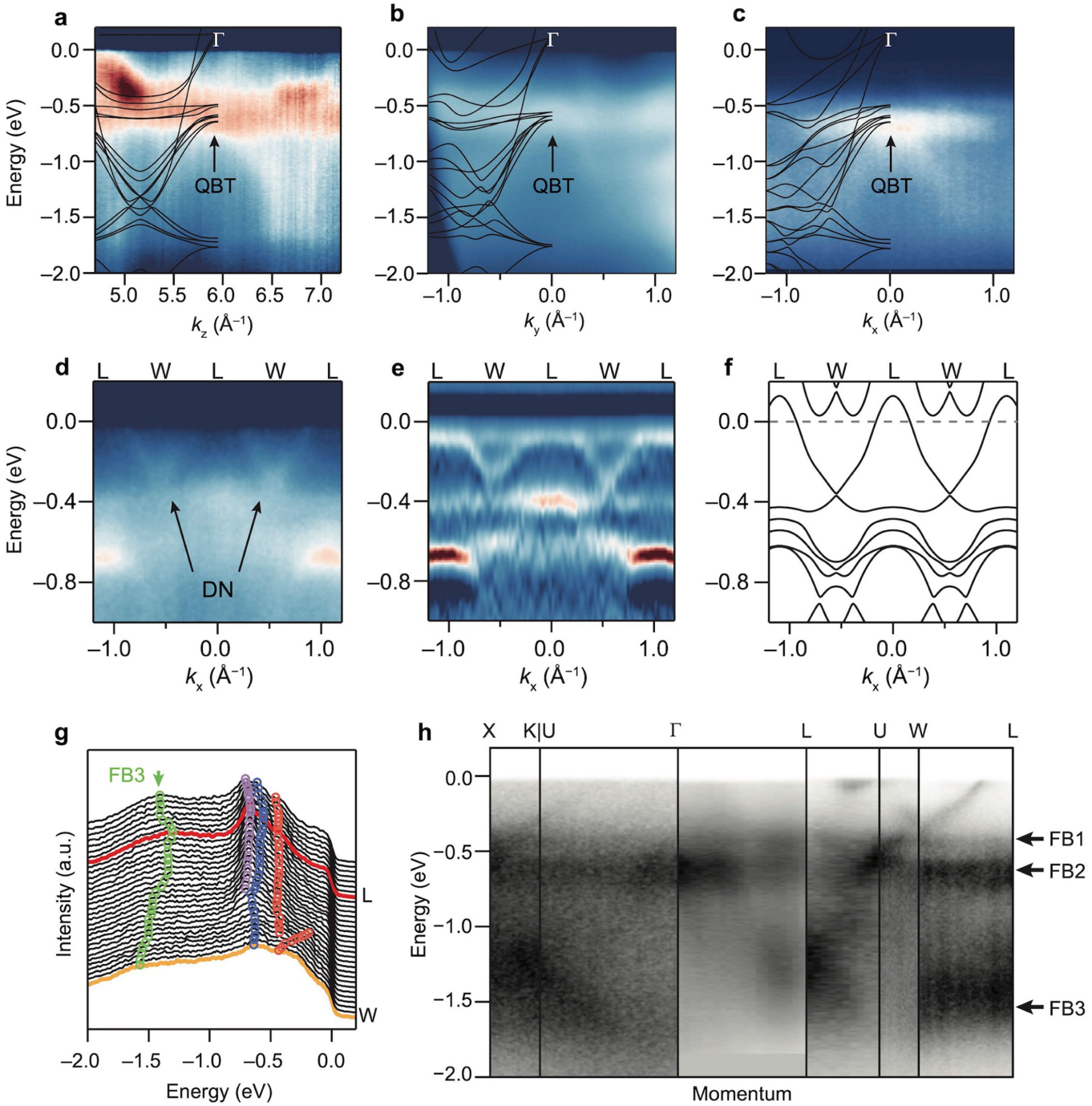

Extended Data Fig. 3 | Pyrochlore band features in $CaNi_2$. (a-c) Dispersion of $CaNi_2$ around the Brillouin zone center Γ. The spectrum in (a) (obtained from the photon energy-dependent ARPES measurements) was normalized using the intensity of the flat band at −0.58 eV. We summed two spectra collected by photons with linear vertical and linear horizontal polarization to minimize matrix element effects. The black arrow marks the quadratic band touching points (QBT) expected from the model pyrochlore tight-binding calculation. (d) ARPES spectrum obtained with 175 eV photons with linear vertical polarization. The black arrows indicate the Dirac nodes at W. (e) Second derivative plot of (d). (f) The DFT band dispersion of $CaNi_2$ to be compared with (d),(e). (g) EDC plots of $CaNi_2$ showing the FB1, FB2, and FB3 dispersions (red, blue, and green circles, respectively). (h) The energy-momentum dispersion along the high symmetry directions. The dispersions along different high symmetry directions were obtained from the following measurements: the Γ-K-X dispersion from the $k_z = 0$ Fermi surface obtained using 217 eV photons, the Γ-L dispersion from the photon-energy dependence measurements from 135 eV to 175 eV photons, and the L-U-W-L dispersion from the $k_z = \pi/c$ Fermi surface obtained using 175 eV photons.

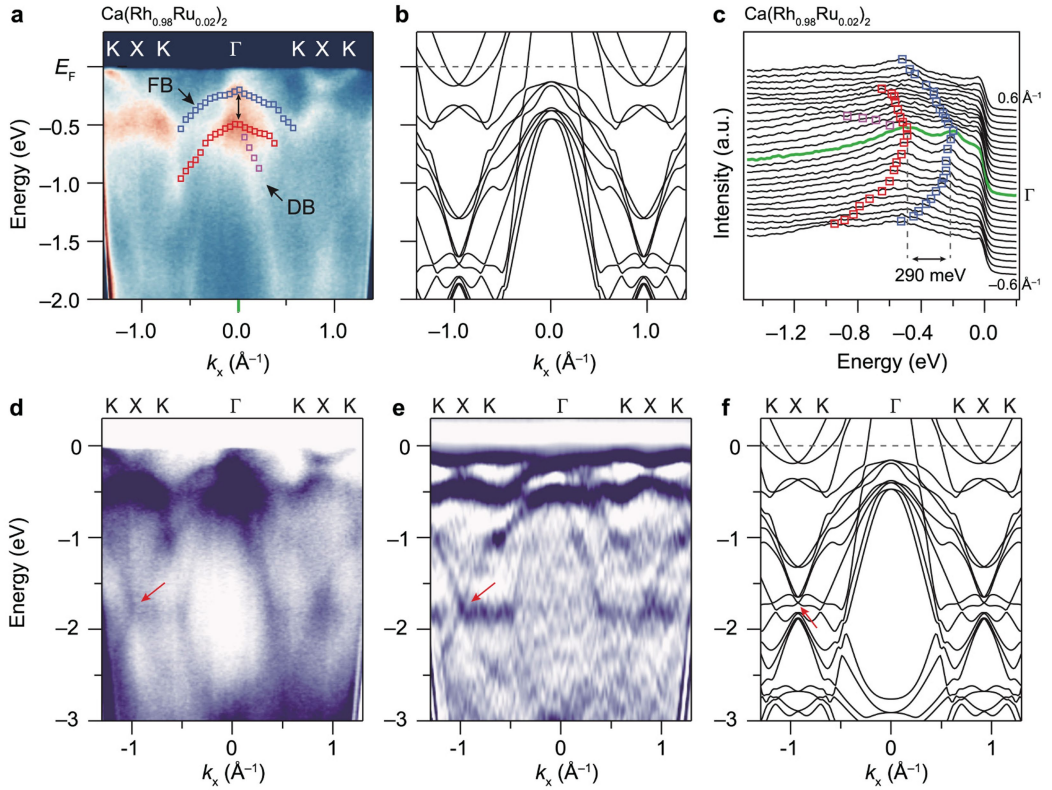

Extended Data Fig. 4 | Topological band features of $CaRh_2$. (a) The ARPES spectrum of $Ca(Rh_{0.98}Ru_{0.02})_2$ along the Γ-K-X direction measured with 127 eV photons. The flat band corresponds to the FB2 in $CaNi_2$ and the dispersive band with band top at Γ are marked with black arrows. Detailed dispersions of the flat band and the dispersive band are obtained from the corresponding EDC analyses in (c) and overlaid on top of the ARPES spectrum in (a). The double-headed arrows in (a) and (c) indicate the SOC gap between the flat band and the dispersive band. (b) DFT band structure of $CaRh_2$ for comparison with the experimental dispersions in (a),(c). (d,e) Wide energy-range ARPES spectrum of $Ca(Rh_{0.98}Ru_{0.02})_2$ and its second derivative plot measured along the Γ-K-X direction. (f) DFT band structure of $CaRh_2$ for comparison with (d,e). The red arrows in (d-f) mark the symmetry-protected Dirac crossing at X.

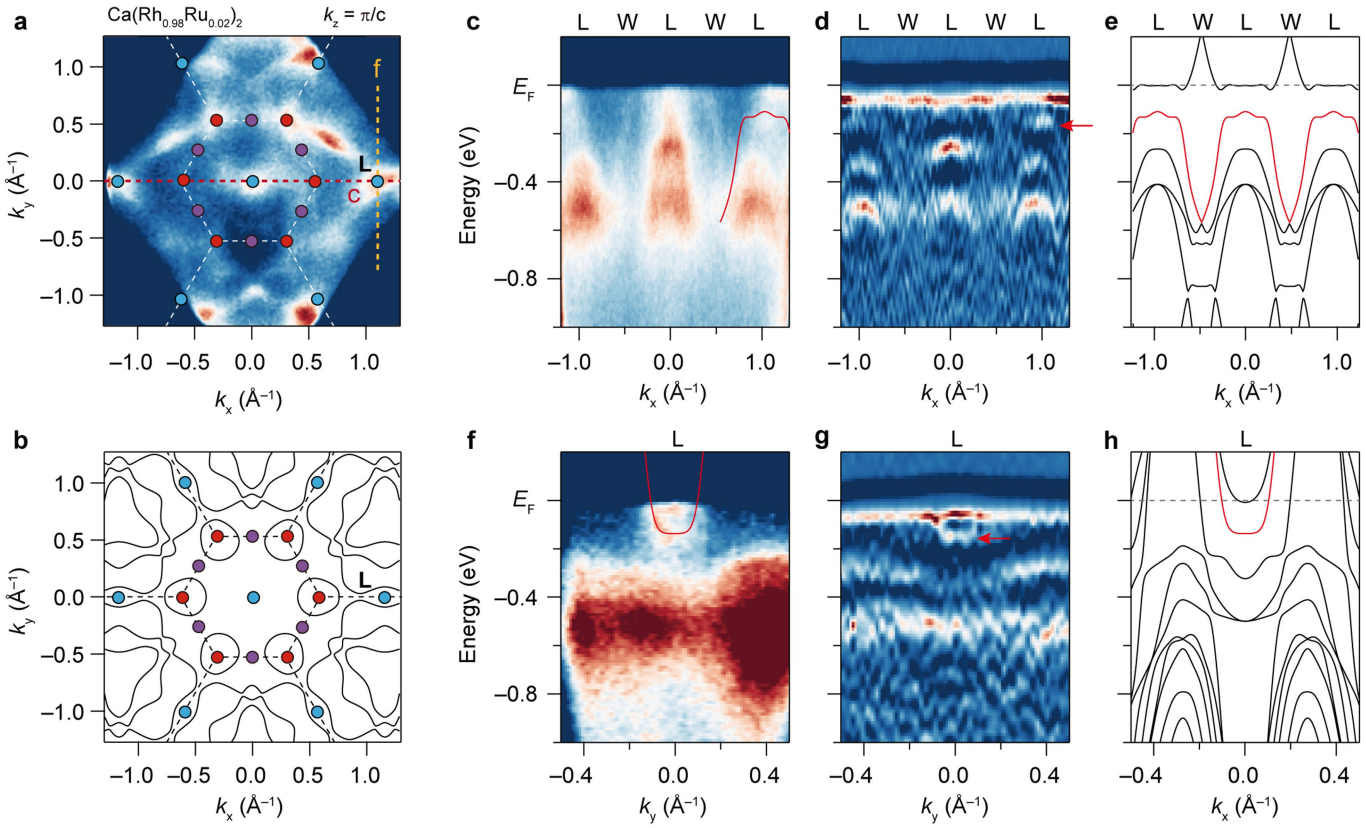

Extended Data Fig. 5 | Saddle point dispersion at L. (a) Experimental Fermi surface of $Ca(Rh_{0.98}Ru_{0.02})_2$. The red and yellow-dashed lines are the momentum directions crossing L point, along which the ARPES spectra in (c) and (f) are acquired, respectively. (b) DFT Fermi surface for $CaRh_2$. (c-e) ARPES spectrum, second derivative plot, and DFT band structure along the k_x direction marked in a. (f-h) Corresponding plots along the k_y direction marked in a. In panels c,f, we overlaid the DFT dispersions to highlight the hole-like band along k_x and the electron-like band along k_y, together forming the saddle point at L. Red arrows in panels d,g also mark the saddle point dispersion. We note that the flat-like features in the second derivative plots are artifacts from the Fermi cutoff. In addition to the saddle point dispersion, we detected an additional highly dispersing band crossing the Fermi level between the L and W in the ARPES spectra of c. This band is not reproduced in the bulk DFT band calculation and is potentially of surface origin.

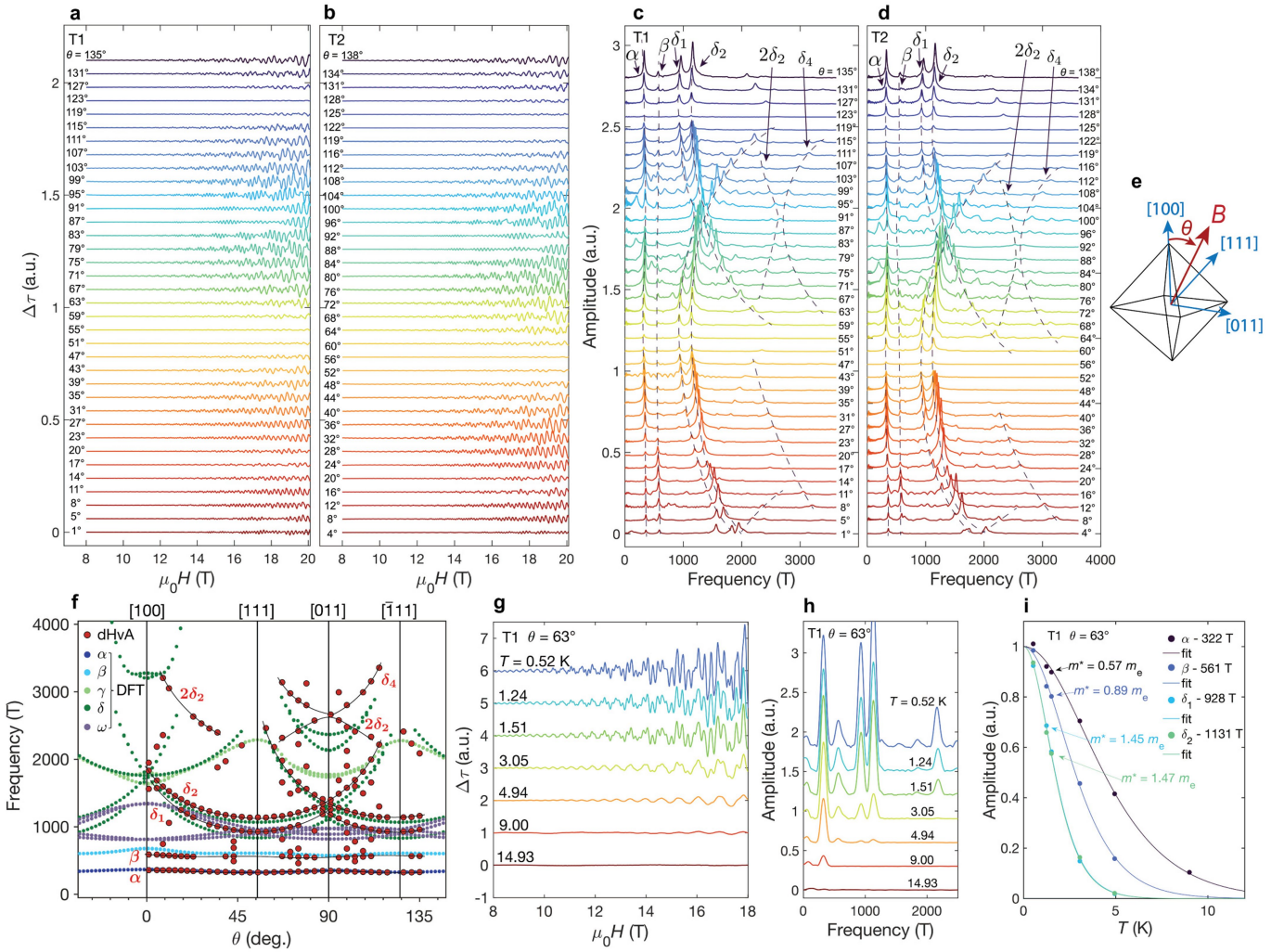

Extended Data Fig. 6 | Quantum oscillations in $CaNi_2$. (a) Polynomial-subtracted magnetic torque data used to extract dHvA frequencies for $CaNi_2$ sample T1 (main) and (b) sample T2 taken at base temperature of the He-3 cryostat. (c,d) Corresponding fast Fourier transform amplitudes (dashed lines are guides to the eye labelled with the orbits identified from calculations). (e) Orientation of θ relative to the crystallographic high symmetry directions for all data in this figure. (f) Observed and calculated quantum oscillation frequencies for $CaNi_2$ as a function of field-tilt angle. (g) Temperature dependent oscillation data taken at $\theta = 63°$ relative to the [100] direction. (h) Corresponding temperature-dependent Fourier transform amplitudes. (i) Temperature dependence of the Fourier transform amplitudes at $\theta = 63°$. Solid lines are fittings to the Lifshitz-Kosevich formula where all 0 K values have been normalized to unity from which corresponding experimental effective mass parameters have been extracted.

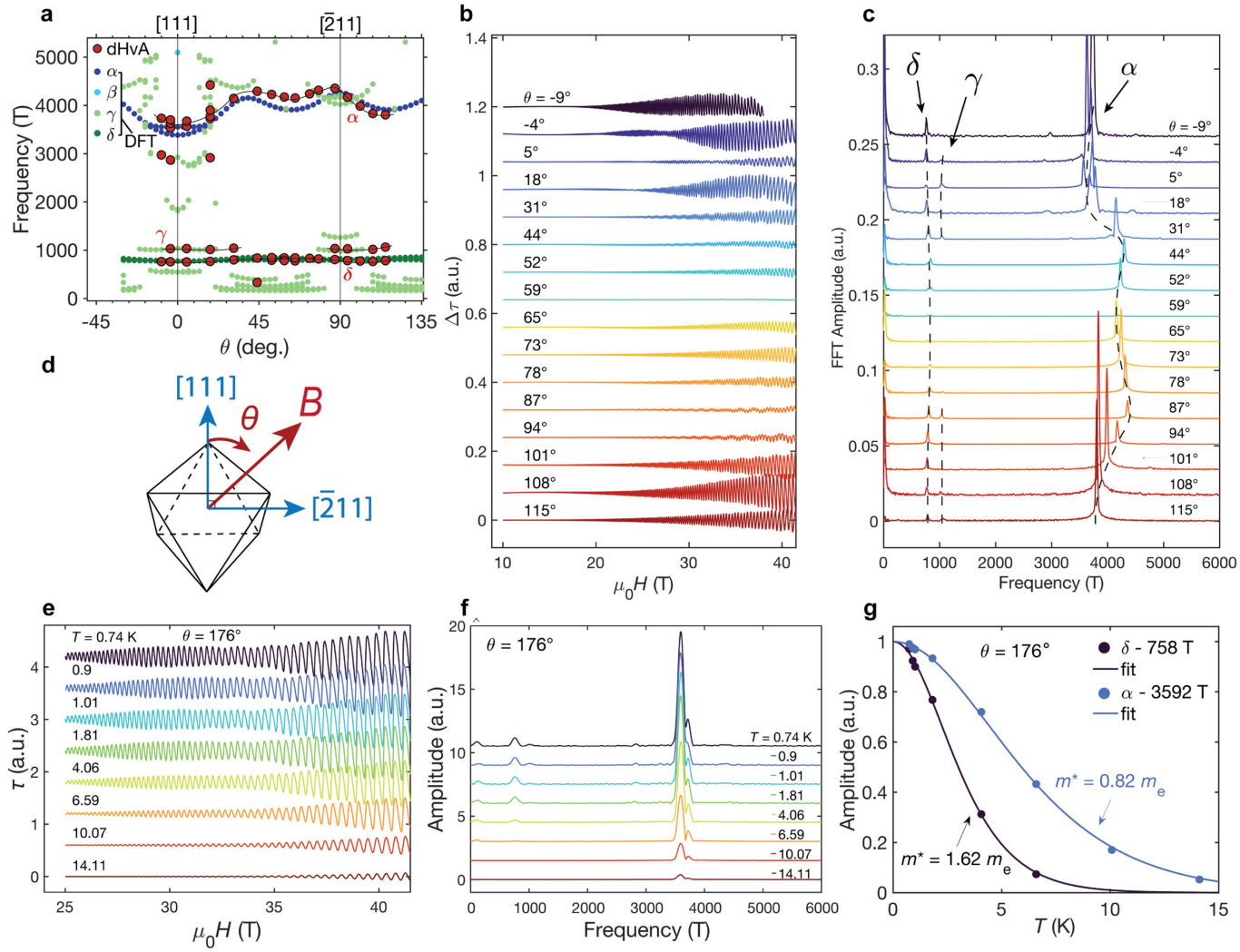

Extended Data Fig. 7 | Quantum oscillations in $Ca(Rh_{0.98}Ru_{0.02})_2$. (a) Observed and calculated quantum oscillation frequencies of $CaRh_2$ as a function of field-angle away from [111], with the geometry as defined in panel (d). (b) Polynomial-subtracted magnetic torque data as a function of field taken at base temperature of the He-3 cryostat, (c) corresponding fast Fourier transform amplitudes (dashed lines are guides to the eye labelled with the orbits identified from calculations). (d) Orientation of θ relative to the crystallographic high symmetry directions, corresponding to the "binary" rotation direction. (e) Temperature dependent oscillation data taken at $\theta = 176°$ corresponding to the [111] direction. (f) Corresponding temperature-dependent Fourier transform amplitudes. (g) Temperature dependence of the Fourier transform amplitudes. Solid lines are fittings to the Lifshitz-Kosevich formula where all 0 K values have been normalized to unity from which corresponding experimental effective mass parameters have been extracted.

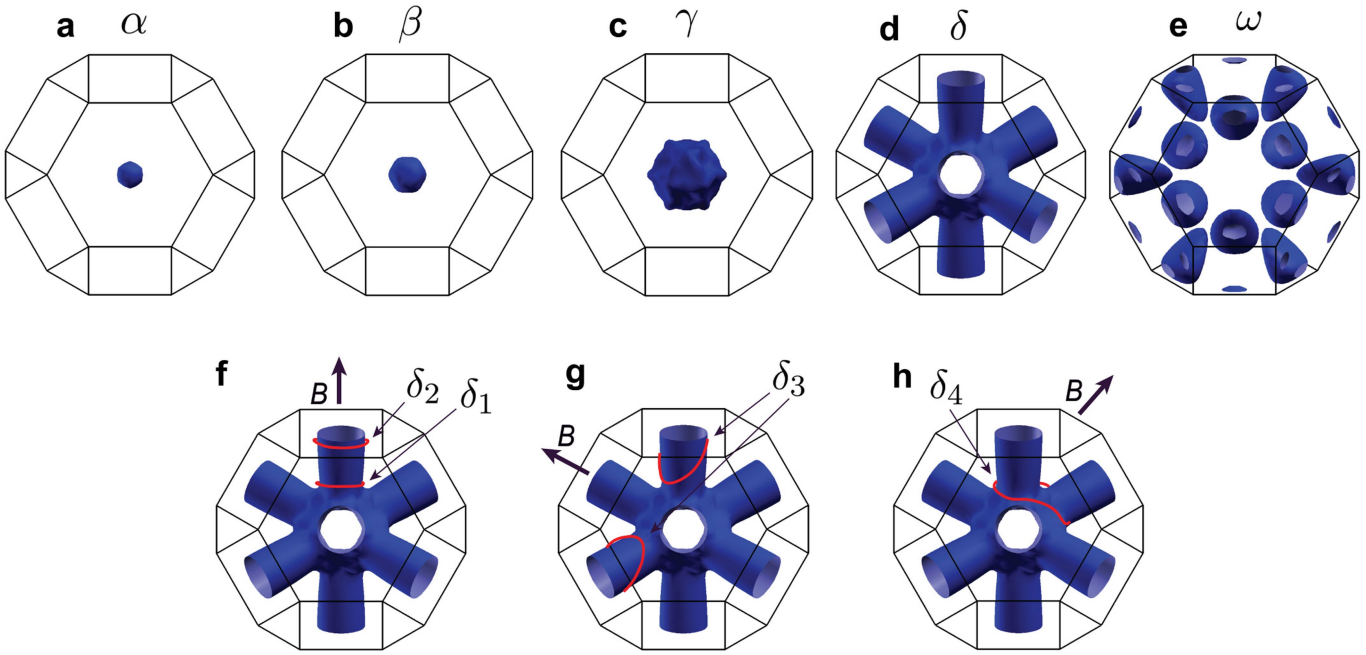

Extended Data Fig. 8 | DFT Fermi surfaces of $CaNi_2$. (a-e) Calculated Fermi sheets of $CaNi_2$ with their corresponding label plotted within one Brillouin zone. (f-h) Schematic showing the locations of characteristic extremal frequencies of the δ Fermi sheet for field along high symmetry directions (f) shows the two lowest frequency branches δ_1 and δ_2 for **B** || [111] (g) δ_3 for **B** || [100], and (h) δ_4 for **B** || [011].

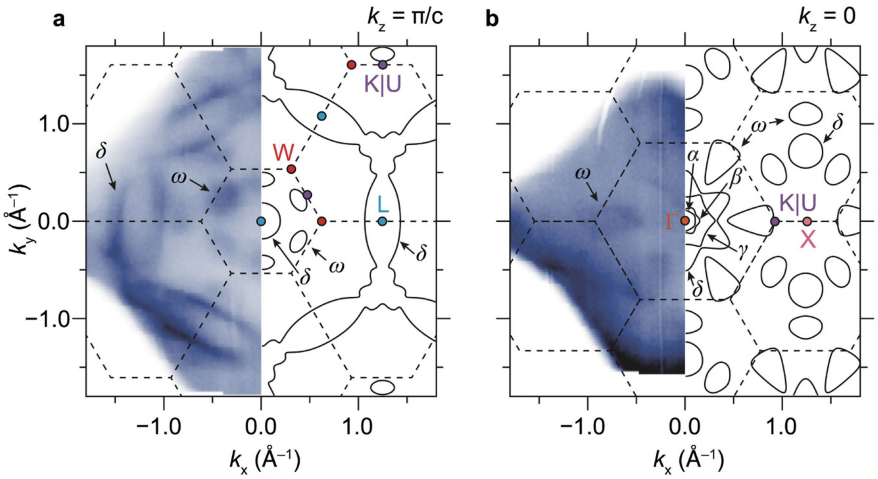

Extended Data Fig. 9 | Fermi surfaces of $CaNi_2$. (a) Fermi surface at $k_z = \pi/c$ and (b) $k_z = 0$. The Brillouin zones are overlaid with black dashed lines. Left and right panels represent the experimental and calculated Fermi surfaces, respectively.

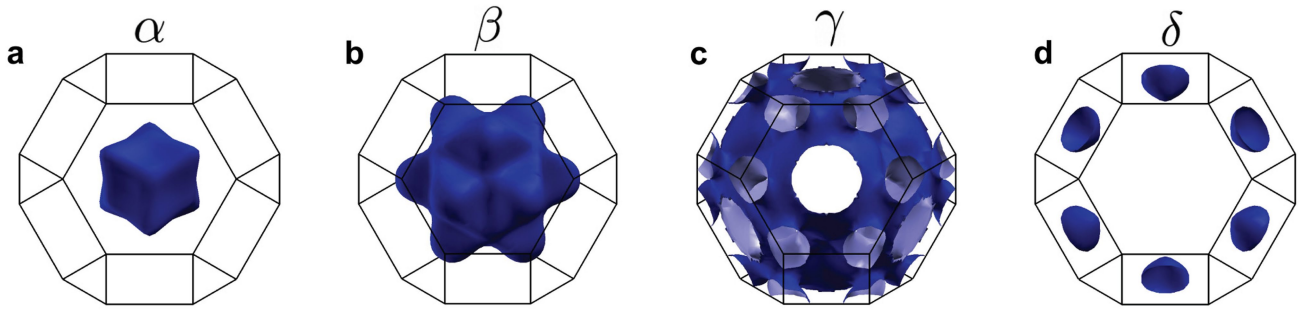

Extended Data Fig. 10 | DFT Fermi surfaces of $CaRh_2$. (a-d) Calculated Fermi sheets of $CaRh_2$ with their corresponding label plotted within one Brillouin zone.